Title

Transcriptional space-time mapping identifies concerted immune and stromal cell patterns and gene programs in wound healing and cancer

Journal

Cell Stem Cell, 30(6)

ISSN

1934-5909

Authors

Hu, Kenneth H
Kuhn, Nicholas F
Courau, Tristan
et al.

Publication Date

2023-06-01

DOI

10.1016/j.stem.2023.05.001

Cell Stem Cell

Resource

Transcriptional space-time mapping identifies concerted immune and stromal cell patterns and gene programs in wound healing and cancer

Graphical abstract

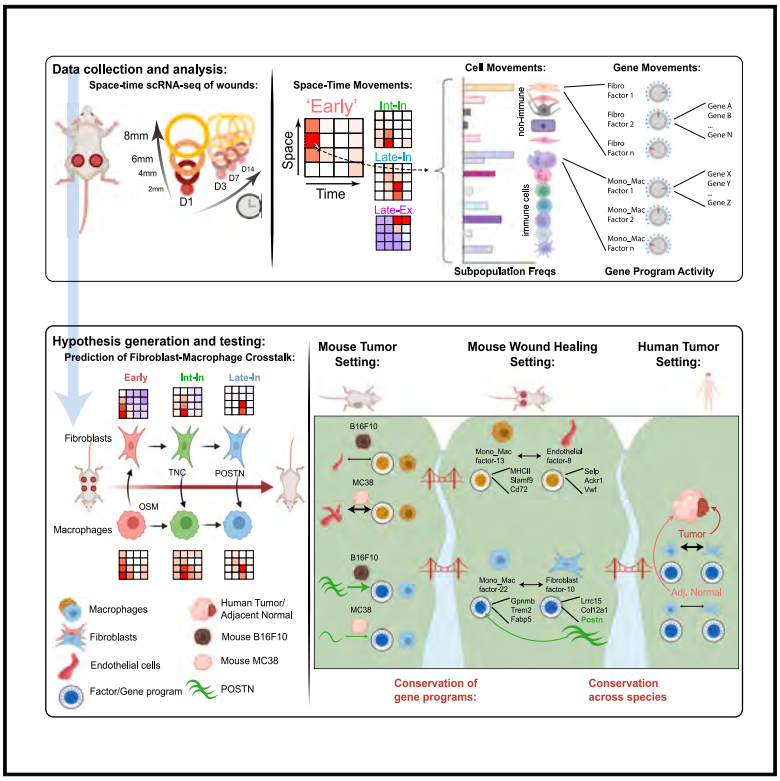

Highlights

- Space-time scRNA-seq of healing skin wounds across immune and non-immune cells
- Gene program analysis reveals coordinated multicellular movements
- Prediction of macrophage-fibroblast crosstalk involving OSM, TNC, and POSTN signals
- Translation of gene program pairs to mouse and human tumor settings

Authors

Kenneth H. Hu, Nicholas F. Kuhn, Tristan Courau, ..., Johannes R. Kratz, Alexis J. Combes, Matthew F. Krummel

Correspondence

khhu@mdanderson.org (K.H.H.), matthew.krummel@ucsf.edu (M.F.K.)

In brief

Hu et al. spatially and temporally dissected cell-cell interactions in the mouse skin wound. Mechanisms of fibroblast-macrophage crosstalk were verified through *in vitro* experiments and imaging. These mechanisms could also be found in tumor samples from mouse models and patients, suggesting that they are conserved units of tissue biology.

Hu et al., 2023, Cell Stem Cell *30*, 885–903
June 1, 2023
https://doi.org/10.1016/j.stem.2023.05.001

CellPress

Cell Stem Cell

CellPress

Resource

Transcriptional space-time mapping identifies concerted immune and stromal cell patterns and gene programs in wound healing and cancer

Kenneth H. Hu,[1,2,6,*] Nicholas F. Kuhn,[1,2,6] Tristan Courau,[1,2,3] Jessica Tsui,[2,3,4] Bushra Samad,[1,2,3] Patrick Ha,[4] Johannes R. Kratz,[2,5] Alexis J. Combes,[1,2,3] and Matthew F. Krummel[1,2,7,*]

[1]Department of Pathology, University of California, San Francisco, San Francisco, CA 94143, USA
[2]ImmunoX Initiative, University of California, San Francisco, San Francisco, CA 94143, USA
[3]UCSF CoLabs, University of California, San Francisco, San Francisco, CA 94143, USA
[4]Department of Otolaryngology Head and Neck Surgery, University of California, San Francisco, San Francisco, CA 94143, USA
[5]Department of Surgery, University of California, San Francisco, San Francisco, CA 94143, USA
[6]These authors contributed equally
[7]Lead contact
*Correspondence: khhu@mdanderson.org (K.H.H.), matthew.krummel@ucsf.edu (M.F.K.)
https://doi.org/10.1016/j.stem.2023.05.001

SUMMARY

Tissue repair responses in metazoans are highly coordinated by different cell types over space and time. However, comprehensive single-cell-based characterization covering this coordination is lacking. Here, we captured transcriptional states of single cells over space and time during skin wound closure, revealing choreographed gene-expression profiles. We identified shared space-time patterns of cellular and gene program enrichment, which we call multicellular "movements" spanning multiple cell types. We validated some of the discovered space-time movements using large-volume imaging of cleared wounds and demonstrated the value of this analysis to predict "sender" and "receiver" gene programs in macrophages and fibroblasts. Finally, we tested the hypothesis that tumors are like "wounds that never heal" and found conserved wound healing movements in mouse melanoma and colorectal tumor models, as well as human tumor samples, revealing fundamental multicellular units of tissue biology for integrative studies.

INTRODUCTION

Metazoans rely on intricate networks of cell-cell crosstalk (CCC) for the maintenance of tissue homeostasis, repair, and regenerative processes after damage.[1–3] Given the diversity of cell types within a tissue, all possible ligand-receptor pairings and their signaling dynamics, a formalized method for interrogating CCC over space and time in the tissue remains a daunting task.[4] Even a minimal two-actor system can exhibit robustness and return to a stable state following perturbation.[5] This same adaptation to perturbation can be seen when increasing the number of cellular actors and, thus, the number of possible "edges" (i.e., CCC axes), such as the combination of stellate cells, hepatocytes, endothelial cells, and Kupffer cells in liver niches.[6]

The advent of single-cell technologies allows profiling of cells on the transcriptional level at resolutions previously unattainable, generating rich datasets identifying highly resolved cell subsets and subtle variations in gene expression and activation states.[7–9] Several computational approaches seek to infer CCC via paired ligand-receptor and target gene expression.[10–12] These inferences are strengthened by applying spatial and temporal context to single-cell transcriptomics that has revealed gene groupings with similar spatiotemporal profiles, shedding light on the spatial segregation of cell functions, the dynamics of cell migration, and tissue zonation.[13,14] Similarly, describing gene expression in terms of spatiotemporal patterns revealed signaling pathways and co-regulation of genes in sub-compartments of liver and pancreas.[15,16] Concordantly, we were motivated to describe the healing skin wound in terms of spatiotemporal multicellular patterns and gene expression programs as skin wound healing (WH) naturally displays well-defined spatial and temporal dimensions. This process has canonically been segmented into major phases with an initial inflammatory response followed by repair/growth and resolution.[17,18] Interspersed are coordinated changes in gene expression patterns in diverse cell types from monocyte/macrophages, neutrophils, fibroblasts, endothelial cells, keratinocytes, and beyond.[3,19] Diverse crosstalk mechanisms between these cell types have been identified for regulating the duration of and transition between phases.[3,19–22] Disruption of these mechanisms often results in aberrant healing, demonstrating the interdependent structure of the WH cellular network.[23,24] Charting the progression of gene expression in single cells over space and time in the wound would yield information on the coordinated behaviors of myriad cell types in an unbiased manner, and how they drive transitions between healing phases.

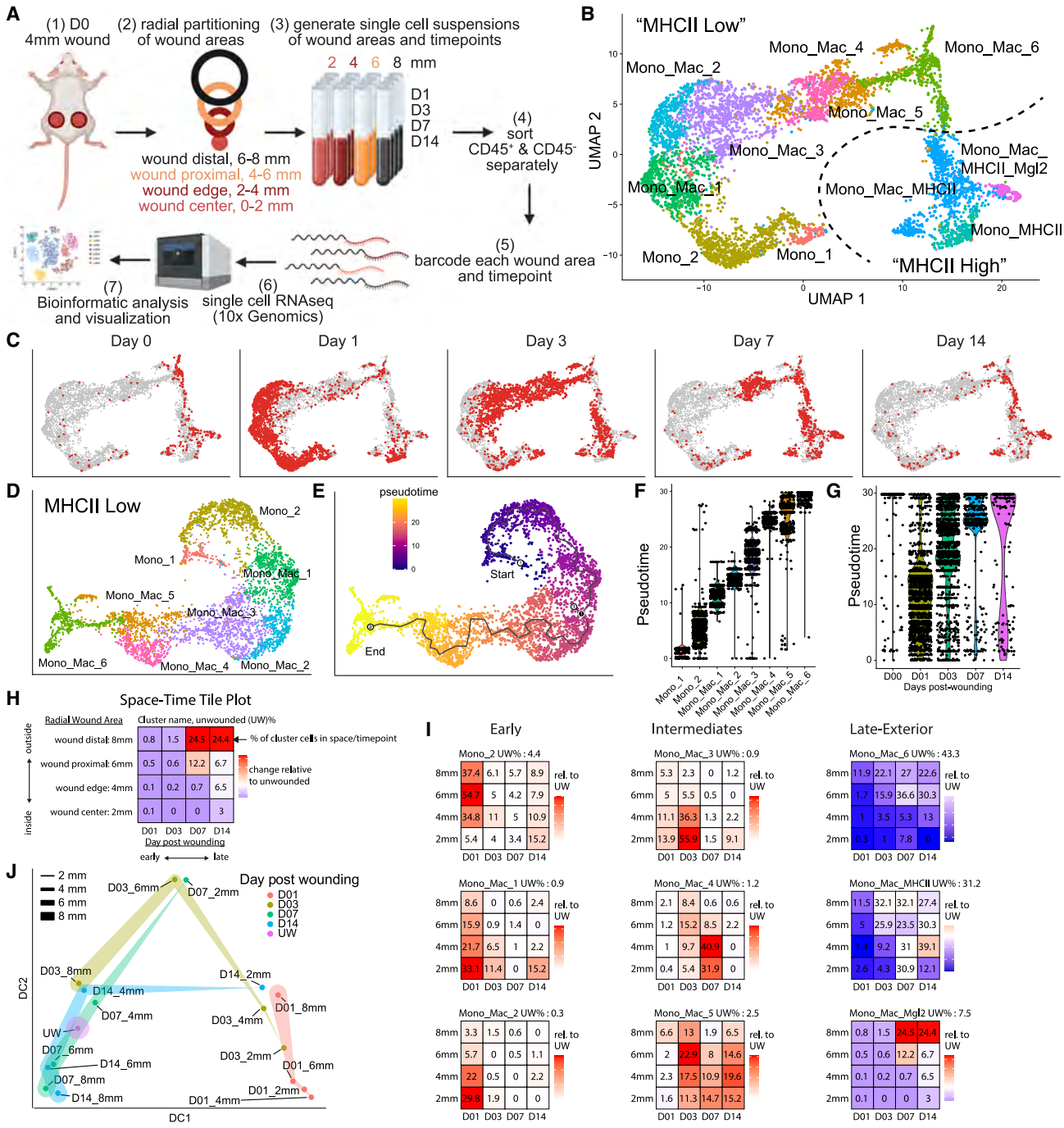

Figure 1. Transcriptional space-time analysis of single cells unveils unique patterns of monocyte/macrophage populations during skin repair

(A) Experimental layout of transcriptional space-time analysis in wounded skin. Cells analyzed from each wound area and time point were pooled from 4 separate wounds. Image generated with Biorender.

(B) Uniform manifold approximation and projection (UMAP) plot of monocyte/macrophage (Mono_Mac) subset from CD45^{+} object. Dotted line separates eight MHCII^{lo} and three MHCII^{hi} Mono_Mac clusters.

(C) UMAP projection of all Mono_Mac cells from (B) in gray and cells highlighted in red by the time point of wound sampling.

(D) UMAP of MHCII^{lo} Mono_Mac subset with eight distinct clusters.

(E) Pseudotime trajectory using Monocle3 on MHCII^{lo} Mono_Mac subset starting at cluster Mono_1, progressing through all cell clusters and ending at cluster Mono_Mac_6.

(legend continued on next page)

With macrophages and fibroblasts representing cell types occupying a continuum of gene expression states,[25,26] as opposed to harboring discrete cell subtypes, clustering approaches are insufficient to capture transitions between states. For example, the M1/M2 ''binning'' of macrophages may represent too reductive a model, as WH macrophages express combinations of canonical M1/M2 genes during all wound phases.[26–29] Therefore, a method for reframing cellular heterogeneity using overlays of gene programs (i.e., collections of co-expressed genes) in the healing wound may better capture the biology underlying the progression of cellular transcriptional heterogeneity.

An additional important rationale for studying space-time progression of multicellular networks relates to chronic disease, where healthy resolution is not achieved. This is exemplified by cancer, where malignant tumor growth co-opts WH programs sans resolution, conceptualized in the idea that tumors are ''wounds that never heal.''[28–30] This idea motivated us to develop a framework based on conserved gene programs to identify if crosstalk elements of the WH cellular network are ''borrowed'' by tumors. The heterogeneity of a given cell type in different contexts may represent a convolution of conserved differentiation, functional, and tissue-specific expression patterns, as seen in resident immune cells scattered across all tissues.[31,32] Describing the common biology between two single-cell datasets may again require going beyond clustering-based approaches that may obscure the identification of overlaid gene programs in a continuum of cell states.[33]

Using skin WH as a well-defined spatial process in tissue repair, we mapped changes in, both, $CD45^+$ and $CD45^-$ cell identity that co-occurred in similar space-time patterns. Layered on the top of cell identity, we identified spatiotemporally expressed gene programs—or factors—that can be grouped based on their unique space-time profile. Because we found these factors based on their shared space-time patterns across multiple cell types, we refer to these co-occurring factors across distinct cell types as multicellular ''gene movements.'' Informed by spatiotemporal profiles of gene program expression, we predicted stromal-macrophage CCC over the time course of wound closure, which we then verified using orthogonal experimental approaches. Finally, we derived a framework for how to identify movements across tissue contexts and identify the conservation of correlated immune and non-immune gene program pairs in mouse tumor models and human tumors. We then validate our predictions to demonstrate the utility of studying conserved gene program groupings.

RESULTS

Separate waves of immune cell infiltration during wound closure

To establish the compositional changes of immune cells during skin repair, we immunophenotyped cells derived from a 4 mm full-thickness circular wound on the mouse's back via Cytometry by time of flight (CyTOF) (Figure S1A). This provided an overview of immune cell populations infiltrating the wound engaging in dynamic remodeling (Figures S1B–S1F). In the dimensional space of our CyTOF panel, the wound temporarily reaches the pre-wound composition at around days 7–10 post wounding and eventually assumes a state that is lymphocyte-rich at day 21 after wounding (Figure S1F; Mendeley Figure S1 at https://doi.org/10.17632/kmmw43j2z6.2). For a deeper dive into space and time, we thus focused upon the first 14 days that encompassed the most dramatic changes.

Transcriptional space-time analysis of single cells unveils unique cell patterns during skin repair

Involvement of both immune and non-immune cells is crucial for skin repair.[34–36] To develop an understanding of how gene expression programs in the different phases of skin repair are linked among cell types, we chose a spatial study across the radial dimensions of a wound. Thus, we radially sampled wounds using successively large punches: wound center (2 mm center diameter), wound edge (2–4 mm diameter), wound proximal (4–6 mm diameter), and wound distal (6–8 mm diameter) (Figure 1A). Given the original wound diameter of 4 mm, we captured two distinct areas within the wound bed plus two distinct areas in skin beyond the wound and into uninjured tissue. These spatial subdomains were collected at time points suggested by the CyTOF study: early inflammatory (day 1 or D01), and then, at successively longer periods of the resolution as suggested by Figure S1E: transition (day 3 or D03), return-to-unwounded (UW) (day 7 or D07), and ''late wound'' (day 14 or D14) (Figure 1A). Upon digestion of the individual rings of tissue, $CD45^+$ immune and $CD45^-$ non-immune cells were sorted separately, barcoded using Multiplexing using lipid tagged indices or MULTI-seq[37] based on their collected time point and area, and then, their transcriptional state assessed by using the 10× Genomics single-cell RNA sequencing (scRNA-seq) platform (Figure 1A). This provided us with a space-time-resolved scRNA-seq dataset by which to query linked gene expression.

Graph-based clustering and differential gene expression analysis of 10,492 $CD45^+$ immune cells revealed heterogeneous monocyte and macrophage subpopulations, neutrophil subpopulations, mast cells, dendritic cells, B cells, T cells, and natural

(F) Violin plot of $MHCII^{lo}$ Mono_Mac subpopulations plotted according to their distribution in pseudotime.
(G) Violin plot of $MHCII^{lo}$ Mono_Mac cells by day post wounding and plotted according to their presence in pseudotime. Day 0 equals unwounded skin.
(H) Outline of space-time tile plot. The 4 × 4 grid depicts relative abundance of a cell cluster across radial wound area (y axis) and time post wounding (x axis). Each tile is one space-time point. Number in tile is the percentage of a subpopulation among all Mono_Mac cells at that specific space time point. Background color indicates relative change compared with unwounded (UW) state: red indicates increase, blue indicates decrease, and white indicates no change in subpopulation compared with UW. Exemplary data are depicted.
(I) Space-time tile plots representing Mono_Mac subpopulations.
(J) Phenotypic earth mover's distance (PhEMD) diffusion map embedding of all space-time points. Each dot represents all $CD45^+$ immune cells captured by scRNA-seq within that space-time point. Dots are color-coded by day and width of band corresponds to area sampled. DC, diffusion coefficient.
See also Figure S1.

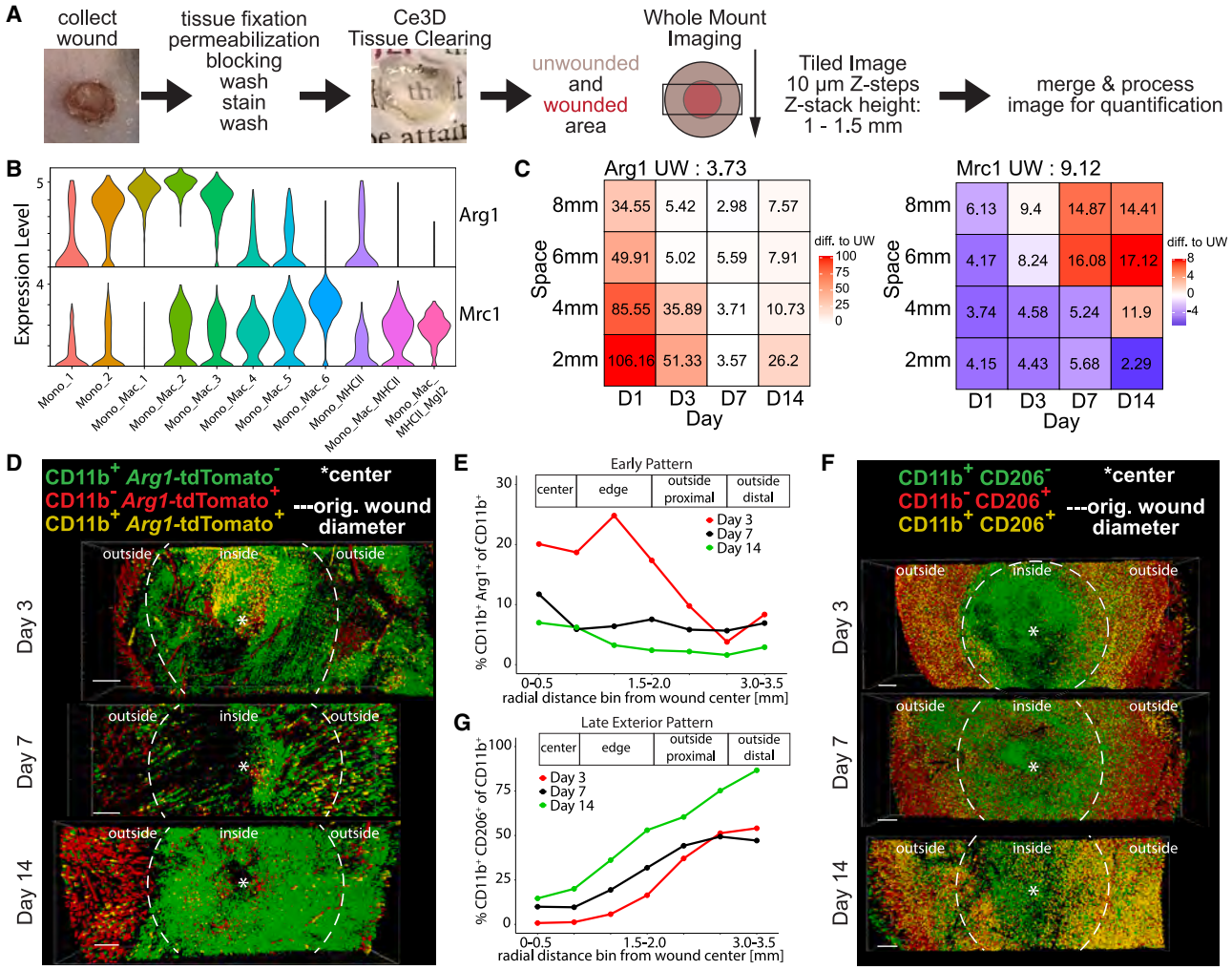

Figure 2. Large-volume imaging visualizes spatial distribution of Mono_Mac subsets in whole wounds during skin repair

(A) Workflow for large-volume imaging. A rectangular cuboid covering the wound and surrounding unwounded skin tissue is acquired on a scanning confocal microscope. Acquired images are stitched together and processed for image analysis using Imaris.

(B) ViolinPlot of (left) *Arg1* and (right) *Mrc1* natural log-normalized mRNA expression level within all Mono_Mac subpopulations.

(C) Space-time tile plot of (left) *Arg1* and (right) *Mrc1* mRNA expression (normalized to depth) within all Mono_Mac cells. Tiles are color-coded relative to unwounded (UW) state. Red, high. Blue, low.

(D) Top-down view of processed image from *Arg1*-reporter mouse on days 3, 7, and 14 post wounding. Colored dots indicate cell location of *Arg1*$^-$ CD11b$^+$ Mono_Mac (green), *Arg1*$^+$ CD11b$^-$ non-myeloid cells (red), and *Arg1*$^+$ CD11b$^+$ Mono_Mac_3 (yellow). Dotted line represents original 4 mm wound diameter. Scale bars, 500 µm. Representative of 2 independent experimental replicates is shown.

(E) Quantification of CD11b$^+$ *Arg1*$^+$ cells in (D) relative to distance from the center of the wound. Percentage of CD11b$^+$ *Arg1*$^+$ of all CD11b$^+$ cells is plotted by day post wounding, representing an early pattern.

(F) Top-down view of processed image on days 3, 7, and 14 post wounding. Colored dots indicate cell location of CD206$^-$ CD11b$^+$ Mono_Macs (green), CD206$^+$ CD11b$^-$ non-myeloid cells (red), and CD206$^+$ CD11b$^+$ Mono_Mac_6 (yellow). Dotted line represents original 4 mm wound diameter. Scale bars, 500 µm. Representative of 2 independent experimental replicates is shown.

(G) Quantification of CD11b$^+$ CD206$^+$ cells in (F) relative to distance from the center of the wound. Percentage of CD11b$^+$ CD206$^+$ of all CD11b$^+$ cells is plotted by day post wounding, representing a late exterior pattern.

See also Figure S2.

killer (NK) cells (Figures S1G and S1H). After re-clustering the monocyte/macrophage (Mono_Mac) populations, we identified three MHCII^{hi} and eight MHCII^{lo} subpopulations (Figures 1B and S1I) and noted that MHCII^{hi} cells expressed markers associated with monocyte-derived dendritic cells (moDCs), such as *Cd209a*[38] and *Nr4a3*[39] (Figure S1I and S1J). With both MHCII^{lo} and MHCI^{hi} Mono_Macs emerging early during WH (Figure 2C, day 1), we reclustered them separately prior to further analysis (Figures 1D and S1K, respectively).

MHCII^{lo} Mono_Macs consisted of two subsets expressing *Ly6c2*, annotated as Mono_1 and Mono_2 (Figure S1I). MHCII^{lo} Mono_Mac_1+2+3 were identified by the transcription factor *Klf2*, which regulates pro-inflammatory cues in monocytes[40] and at least one of the chemokines *Cxcl3*, *Ccl2*, *Ccl6*, *Ccl7*, and

Ccl24. Finally, Mono_Mac_4+5+6 shared *Ms4a7* and *Apoe* expression, two markers associated with microglia and brain-border macrophages.[41,42] Using pseudotime analysis,[43] we anchored a trajectory on Mono_1+2 populations, representing cells most similar to Ly6C^{hi} blood-circulating monocytes (Figure S1I), which then proposed a linked transcriptional progression through all clusters successively, eventually ending at Mono_Mac_6, putatively the most terminal Mono_Mac cluster (Figures 1E and 1F). Consistent with this interpretation, Mono_Mac MHCII^{lo} cells from different time points map along the calculated pseudotime (Figure 1G) with the exception that cells collected on day 14 were split between early and late pseudotime, highlighting the status of the late wound as a distinct state from UW and "early wound" states that was also found in the CyTOF data (Figure S1F). Leveraging this trajectory, we also found the trends of gene expression of known myeloid cell states: early expression of inflammatory gene *Ly6c2*,[44] mid-point expression of *Slpi* and *Mmp12*, with *Mmp12* being linked to antagonizing further monocyte recruitment,[45] and late expression of *Mrc1*, associated with tissue-resident macrophages (Figure S1L).

To search for patterns of space-time distribution of myeloid states, we created tile plots in which each tile shows the prevalence of a cell population—defined from the clustering, above—relative to the UW state, both over time (x axis) and space (y axis) (Figure 1H). We discovered greater spatial complexity in how specific immune populations emerge through WH phases (Figure S1M), exemplified by the Mono_Macs (Figure 1I). Three subpopulations were characterized as "Early" (i.e., peak at day 1)—represented by Mono_2, Mono_Mac_1, and Mono_Mac_2 and varied from 6 to 2 mm in the peak location of the amplified population. Three others had middle-originating waves (day 3 or day 7): denoted as "intermediates" and represented by Mono_Mac_3+4+5. Each of these again had specific space-time patterns of recruitment, with Mono_Mac_2 exhibiting an "intermediate interior (Int-In)" and Mono_Mac_4 a "late interior (Late-In)" pattern. Three others had "late exterior (Late-Ex)" distributions, namely Mono_Mac_6, Mono_Mac_MHCII, and Mono_Mac_MHCII_Mgl2, and these were noted as "return" populations, namely that the frequencies dipped and then returned to levels in the UW state (Figure 1I). Notably, the earliest progenitor Mono_1, as well as Mono_MHCII, did not fit into those patterns (Figure S1N).

Our spatial scRNA-seq dataset also captured the space-time accumulation of additional immune cells beyond monocytes and macrophages (Figure S1M). Using phenotypic earth mover's distance (PhEMD) analysis, the samples occupied an arc-like trajectory in reduced dimensions (Figure 1J), similar superficially to that seen in CyTOF bulk analysis in Figure S1. In this analysis, late wound outside areas (day 7_6 mm, day 7_8 mm, day 14_6 mm, and day 14_8 mm) are more like each other than the UW state, again supporting the previous observation that the immune composition reaches a late wound state after skin repair, dissimilar to pre-injury (Figures 1J and S1F).

Large-volume imaging visualizes the spatial distribution of Mono_Mac subsets in wounded skin

We aimed to validate our gene expression patterns via large-volume tissue imaging to probe for the localization of individual cell states (Figure 2A). The clearing-enhanced 3D (Ce3D)[46] protocol allowed detection of immune and non-immune cells within wounded skin, highlighting their relative position to the wound edge as marked by integrin alpha-6 (ITGA6) staining of the re-established epithelial basement membrane (Figure S2A; Video S1, white). Of note, ITGA6 staining also highlighted vasculature structures in non-wounded skin, hair follicles, fascia, and severed nerve bundles lying outside of the closing wound (Figure S2B; Video S2, white).

We focused on two markers, *Arg1* and CD206/*Mrc1*, that, although often grouped together as a combined signature of "M2" macrophages *in vitro*,[47] show clear cell subset (Figure 2B) and space-time distinct (Figure 2C) patterns in WH, further confirming results from tumors[48] that they are not obligately part of the same gene network. By scRNA-seq data, early inflammatory Mono_Mac subpopulations Mono_Mac_1+2+3 express high levels of *Arg1* (Figures 2B and S2C). We validated this via cleared wound images using an *Arg1* reporter mouse,[49] finding that CD11b^{+} *Arg1*$^{+}$ myeloid cells were predominantly found at the center of wounds and at early but not late time points after wounding (Figures 2D, 2E, and S2D–S2F; Videos S3 and S4), consistent with the space-time tile plot (Figure 2C). Confirming previous data,[50] we also detected *Arg1*$^{+}$ CD11b^{-} hair follicles in UW skin (Figures S2E and S2G). Conversely, *Mrc1* expression was highest in the Mono_Mac_6 subpopulation and predominated in exterior wound regions late (Figures 2B, 2C, and S2H). Large-volume imaging probing for *Mrc1*-encoded protein CD206 confirmed the absence of CD11b^{+} CD206^{+} cells in the center of the wound on day 3 post wounding (Figure 2F) and their increased abundance on the exterior non-wounded skin area across all time points measured (Figures 2G and S2I–S2K; Videos S1 and S2), proving the veracity of our space-time scRNA-seq mapping.

Unique space-time patterns of fibroblast subpopulations have matching Mono_Mac patterns

Building on these space-time patterns, we focused on other cell types with matching patterns. Unsupervised clustering of 6,944 CD45^{-} cells identified 19 different clusters, separated into endothelial cells, fibroblasts, melanocytes, muscle cells, keratinocytes, and dermal sheath papilla cells (Figures 3A and S3A). Akin to immune populations, fibroblasts (Figures 3B–3D) and other skin-resident cells (Figure S3B) displayed distinct space-time distributions. To seek matched patterns, we primarily focused on fibroblasts as their interaction with macrophages is well documented.[51] Here, we identified 5 separate fibroblast clusters by distinct gene expression (Figures 3B and S3C) and initially numbered them in accordance with their accumulation in time during skin WH (Figures 3C and 3D).

The Fibro_1 cluster was annotated as "inflammatory" due to high expression of inflammatory mediators (Figures S3C and S3D)[52,53] and their emergence on day 1, representing more than 50% of all wound fibroblasts at that moment (Figure 3D). The Fibro_3 and Fibro_4 clusters expressed genes associated with collagen production and cell contraction (Figures S3C and S3D)[53–55] and were annotated as "early myofibroblasts" and "myofibroblasts," respectively. Their space-time profile revealed they make up about 50% of all fibroblasts on days 3 and 7 in the inner regions of the wound (Figure 3D). By day 14, the myofibroblasts have returned to UW levels (Figure 3D), highlighting their resolution on completed skin healing.

With the Fibro_2 cluster showing transcriptional similarity to previously described "universal" and "immunomodulating"

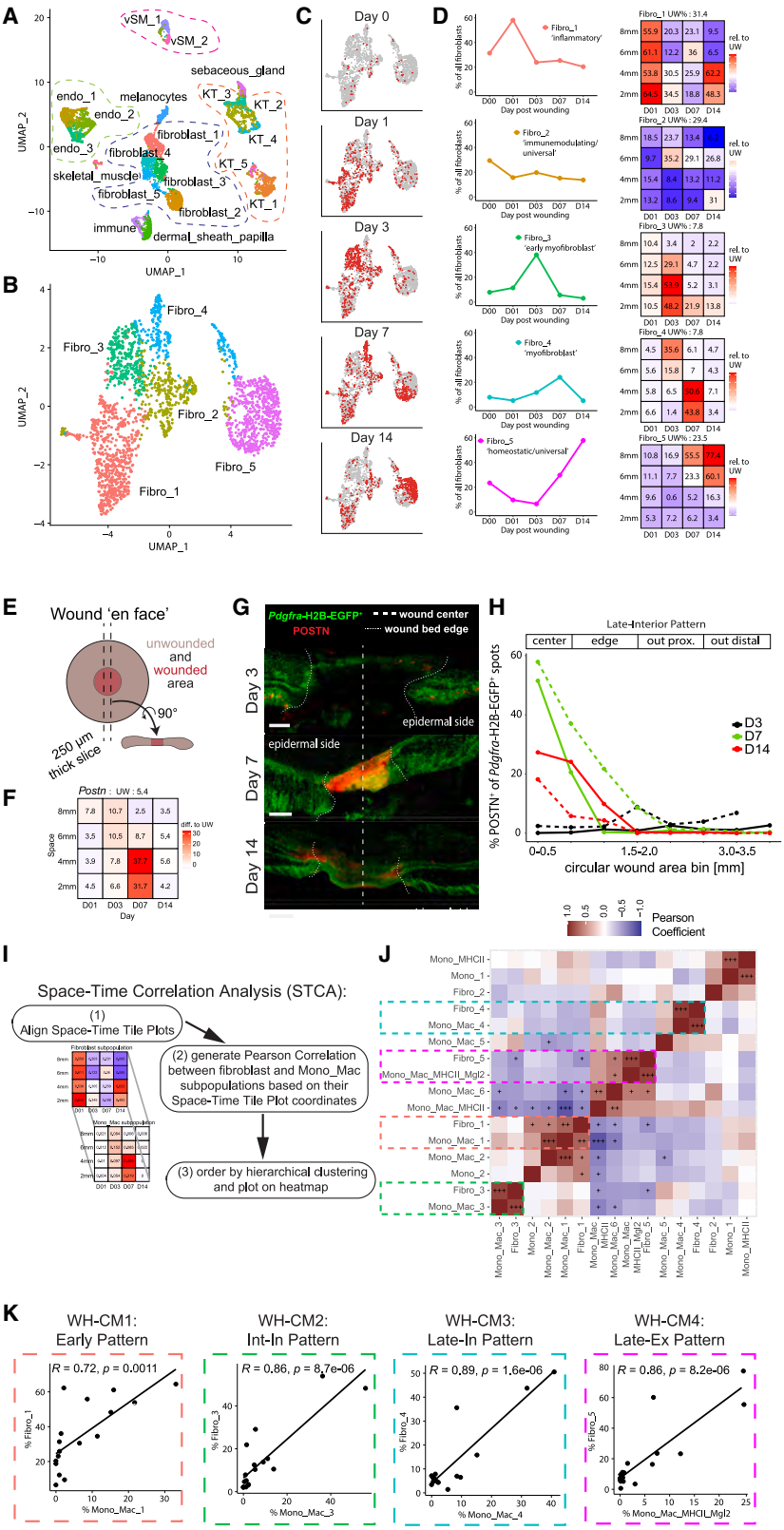

Figure 3. Unique space-time patterns of fibroblast subpopulations have matching Mono_Mac patterns

(A) UMAP plot of CD45^{-} non-immune cells during skin repair. Endo, endothelial cells. KT, keratinocyte; vSM, vascular smooth muscle.

(B) UMAP plot of the fibroblasts during skin repair.

(C) UMAP projection of all fibroblasts from (B) in gray and cells highlighted in red by time point of wound sampling.

(D) Left: line plots of fibroblast subpopulations identified in the scRNA-seq dataset during skin repair. Percentage of each subpopulation within all fibroblasts plotted by day post wounding. Right: space-time tile plot representing fibroblast subpopulations. Each tile is one space-time point. Number in tile is percentage of subpopulation among all fibroblasts at that specific space-time point. Color indicates relative change compared with unwounded (UW) state. Red indicates increase and blue indicates decrease in subpopulation compared with UW.

(E) Schematic depicting wound "en face" imaging. A 250 μm thick cross-section of fixed wound tissue is collected, stained, cleared using Ce3D, and the whole volume is imaged by scanning confocal microscopy.

(F) Space-time tile plot of *Postn* mRNA expression (normalized to depth) within fibroblasts. Tiles color-coded relative to unwounded (UW) state. Red, high; blue, low.

(G) 3D-views of dorsal skin wound cross-sections from *Pdgfra*-reporter mice collected at days 3, 7, and 14 post wounding. Periostin (POSTN) protein staining shown in red. Dotted vertical line, day 0 wound center. Scale bars, 500 μm.

(H) Quantification of *Pdgfra*-H2B-EGFP^{+} spots proximal to POSTN^{+} staining as a percentage of all *Pdgfra*-H2B-EGFP^{+} spots in (G) relative to distance from the center of the wound. Percentage of POSTN-proximal *Pdgfra*-H2B-EGFP^{+} spots are plotted by day post wounding representing a late-interior pattern. Two independent experiments shown overlaid with line dashes representing each replicate.

(I) Outline of space-time correlation analysis (STCA).

(J) Pearson correlation matrix output of STCA comparing fibroblast and Mono_Mac subpopulations. Correlation was calculated using Pearson correlation and significance adjusted for multiple comparisons using Bonferroni-Hochberg (BH) correction. +p value < 0.05, ++p value < 0.005, +++p value < 0.0005.

(K) Correlation xy-plots of select fibroblast-Mono_Mac subpopulation pairs displaying high Pearson correlation in occurrence in space-time during wound skin repair, as identified in (J). Each dot represents one space-time point, i.e., one tile from the space-time tile plot and the unwounded state. The percentage of each paired fibroblast and Mono_Mac cluster within the whole fibroblast or Mono_Mac population, respectively, is plotted for each space-time point. Pearson correlation test used to calculate correlation coefficient R and p value. WH-CM, wound healing cell movement; Int-In, intermediate interior; Late-In, late interior; Late-Ex, late exterior.

See also Figure S3.

fibroblasts and the Fibro_5 cluster displaying similarity to "homeostatic/universal" fibroblasts (Figures S3C–S3F),[56,57] they were annotated as such. Of all the identified fibroblast subsets, the "immunomodulating/universal" Fibro_2 remained the steadiest in both space and time (Figure 3D), whereas the homeostatic/universal Fibro_5 constitute 23.5% of all fibroblasts in UW skin and increase over time to reach baseline levels by days 7/14 (Figure 3D). Finally, the Fibro_5 dominated the fibroblast population outside of the wounded area (6–8 mm), making up 55%–77% of all fibroblast cells there (Figure 3D). This highlights the effect of local wound repair on neighboring UW skin areas, where cell compositions are affected, despite the tissue not being subject to direct physical injury.

To visually validate the space-time patterns of fibroblast subsets, we collected wounds at different time points post wounding and generated 250-micron thick wound sections spanning the wound for staining and cleared via Ce3D (Figure 3E) after staining for periostin (POSTN) and α-smooth muscle actin (αSMA), as markers for the myofibroblast-like Fibro_4 and Fibro_3 subsets, respectively (Figures S3C and S3D). In our scRNA-seq dataset, *Postn* and *Acta2* (the gene encoding αSMA) have distinct space-time expression patterns within fibroblasts, with *Postn* being most prevalent in the center of the wound on day 7 (Figure 3F) and *Acta2* emerging on day 3 and then being more focused in the center of the wound at later time points (Figure S3G). Using *Pdgfra*-reporter mice to mark fibroblasts,[58] we validated the scRNA-seq space-time pattern of *Postn* on the protein level present in the center of the wound on day 7 and markedly reduced day 3 and day 14 (Figures 3G and 3H). The position of αSMA^{+} fibroblasts cells not associated with vascular smooth muscle (vSM) (example in Figure S3H) in the wound over time mirrored the scRNA-seq space-time pattern of *Acta2*: prevalent on the outside on day 3 and then detectable in the center on days 7 and 14 (Figures S3I and S3J). This corroborates the space-time tile plot patterns of the myofibroblast-like Fibro_3+4 subsets and their dynamic appearance and disappearance during the WH process.

With the cell states of two key populations (fibroblasts and Mono_Macs) mapped across WH space-time (Figures 1 and 2), we asked whether they co-occurred during the WH process, highlighting groups of heterotypic cell types putatively engaged in CCC. We performed a space-time correlation analysis (STCA) of the fibroblast and Mono_Mac subpopulations across the tile plot (Figure 3I; see STAR Methods for further details). This uncovered four co-occurring Mono_Mac/fibroblast pairs with very high degrees of space-time correlation, namely: inflammatory Fibro_1 and Mono_Mac_1, early myofibroblast Fibro_3 and Mono_Mac_3, myofibroblast Fibro_4 and Mono_Mac_4, and homeostatic/universal Fibro_5 and Mono_Mac_MHCII_Mgl2 (Figure 3J). To visualize this in another way, we plotted cell percentages for each of these subpopulations over all samples and found high cross-correlations throughout the WH process (Figure 3K), with the Fibro_1 and Mono_Mac_1 pair coinciding as an Early WH cell movement 1 (henceforth, WH-CM1), Fibro_3 and Mono_Mac_3 representing the "Int-In" pattern (WH-CM2), Fibro_4 and Mono_Mac_4 representing the "Late-In" pattern (WH-CM3), and Fibro_5 and Mono_Mac_MHCII_Mgl2 representing the "Late-Ex" pattern (WH-CM4) (Figures 1I and 3D).

A larger STCA analysis, comparing all identified $CD45^{-}$ non-immune and $CD45^{+}$ immune cell subpopulations in our spatio-temporal scRNA-seq dataset, demonstrated a 5th cluster of correlation (Figure S3K; Table S1). This block is only represented by endothelial cells, DCs, and NK cells and represents an "Edge" cell movement (WH-CM5) (Figure S3K). The distinct meanings for some of these additional cell types will await further in-depth analysis as, in this study, we next sought to dive deeper into the gene expression programs that might link two candidate cell types and underlie the pattern of their CCC.

Gene program analysis identifies movements of gene expression across diverse cell types and predicts cell-cell interactions between macrophage and fibroblasts

Moving beyond cluster-based analysis, we applied non-negative matrix factorization (NMF). This analysis seeks to decompose a cell by gene matrix into the product of two smaller matrices with non-negative components[59,60] and can reveal layers of heterogeneity beyond clustering, especially in a population of cells without clearly demarcated subpopulations.[33,61,62] Here, collections of genes with similar expression patterns across the cell type contribute to a "factor" with their gene weight denoting the strength of its contribution to that factor (Table S2). Each cell is also then assigned a loading value for each factor (e.g., feature plots in Figures 4A and 4B), which can also be visualized in space-time (tile plots in Figures 4A and 4B). We henceforth use the terms factor and "gene program" interchangeably.[61,63]

We applied a variation of NMF analysis, termed non-smooth NMF (nsNMF),[64] to our fibroblast and macrophage subset because of its sparser output during factorization compared with the base NMF algorithm.[64,65] We applied a cophenetic metric to identify the optimal number of factors as in Figure S4C.[66] This resulted in 24 factors for all Mono_Mac populations and 17 factors for the fibroblasts, each with a largely unique and specific collection of top contributing genes (Figures S4A and S4B). Some genes are shared strongly between factors. For example, MHCII-associated genes (e.g., *H2-Aa* and *H2-Ab1*) are shared between Mono_Mac factor-4 and factor-7 (Figure S4A); however, such overlaps remain rare.

Like the STCA above with cell subpopulation fractions, we asked if the space-time patterns of certain factors in the Mono_Mac population were correlated with factors in the fibroblasts. Using a similar approach to Figure 3I, we identified pairs of strongly correlated Mono_Mac and fibroblast factors. We focused on three sets of correlated factors—henceforth, gene movements (GMs): WH-GM-1 through 3. These, respectively, exhibit space-time patterns broadly similar to WH-CM1 (Early), WH-CM2 (Int-In), and WH-CM-3 (Late-In) patterns described above (see Figure 4C and tile plots in Figures 4A and 4B).

Based on the space-time coincidence of these factors, we explored the hypothesis that such correlations could reveal cell-cell signaling between fibroblasts and Mono_Macs that drive the emergence of reciprocal gene programs over the time course of wound closure (Figure 4D). We began by examining fibroblast/Mono_Mac movements WH-GM-1 through 3 using CellChatDB[10] to help identify putative ligands that are products of genes contributing to a "sender" factor (Figure S5D; Mendeley Figure S4 at https://doi.org/10.17632/kmmw43j2z6.2). We then

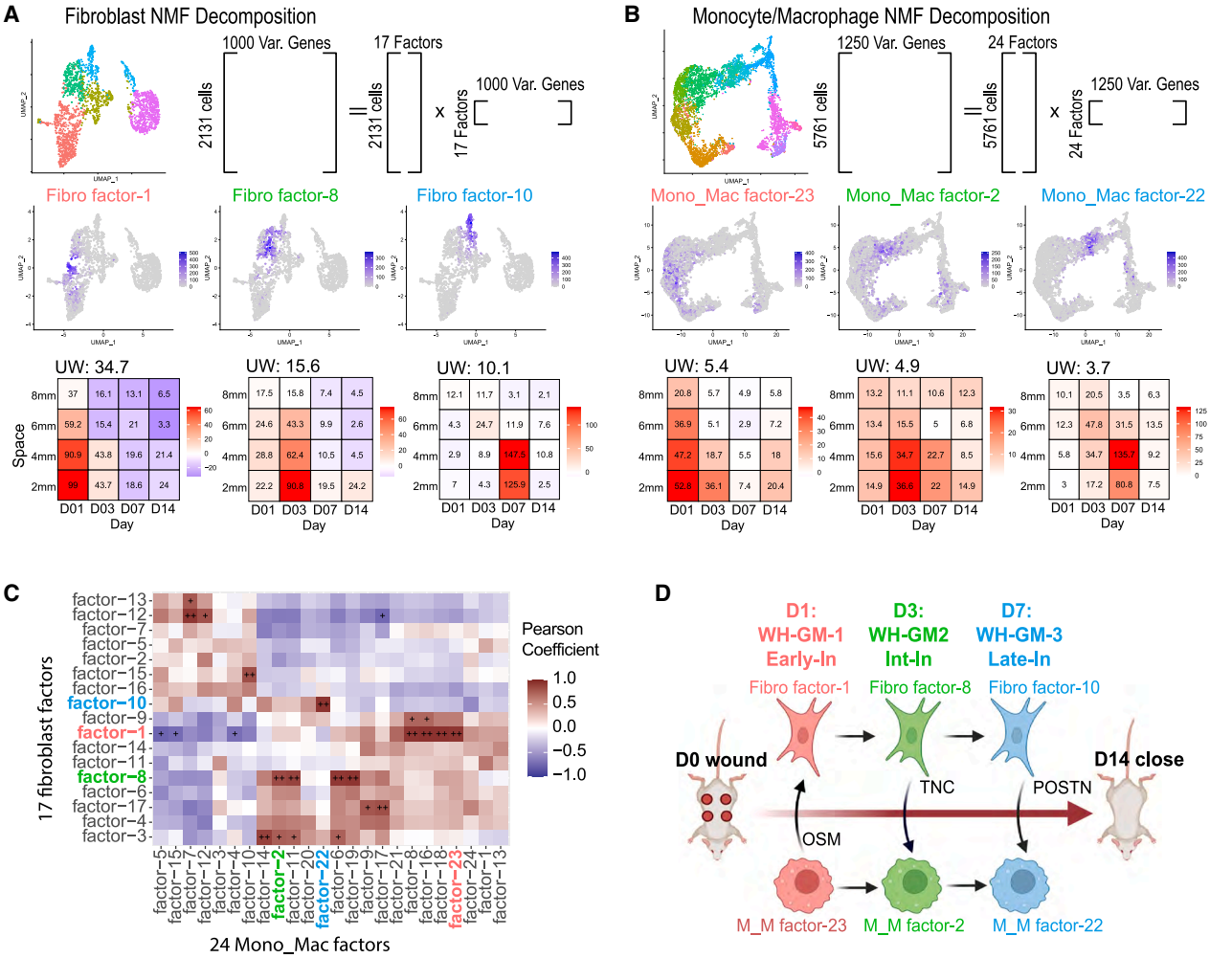

(legend on next page)

experimentally queried if the set of top contributing genes of the correlated "target" factor, in the opposite cell type, might be upregulated by the ligand of interest. We explored three such relationships between macrophages and fibroblasts as follows.

WH-GM-1/Early-In: the oncostatin M (OSM) pathway was predicted by CellChat to be most prevalent at day 1 (Figure S4D) with *Osm* being a major contributing gene to Mono_Mac factor-23 (Figure S4A). This, in turn, was defined to be in a space-time GM with fibroblast factor-1 (Figure 4C). We then used real-time quantitative PCR to test how *in vitro* stimulation with OSM would affect gene expression in primary skin fibroblasts (PSFs), finding that genes shown in Figure S4B that contribute most heavily to fibroblast factor-1 (e.g., *Serpinb2*, *Serpine1*, *Bnip3*, and *Glul*) were significantly upregulated by OSM treatment (Figure 4E). Importantly, top contributing genes to other factors (e.g., *Acta2*, *Cygb*, and *Postn*) were not similarly upregulated, indicating the specificity of the predictions generated from NMF analysis.

WH-GM-2/Int-In: we noted the emergence of Mono_Mac factor-2 at day 3 in the interior of the wound, coinciding with fibroblast factor-8 (Figure 4C). *Tnc* encoding tenascin-C (TNC) was a major contributing gene to fibro factor-8 and is known to skew macrophage polarization.[67] We predicted the exposure of bone marrow-derived macrophages (BMDMs) to TNC would upregulate the suite of top contributing genes to Mono_Mac factor-2. We found that genes that strongly and specifically contributed to Mono_Mac factor-2 (e.g., *Cd83*, *Ccrl2*, *Id3*, *Gadd45b*, and *Tgif1* among others) were upregulated following TNC treatment (Figure 4F).

WH-GM-3/Late-In: CellChat predicted the POSTN pathway for day 3/day 7 could signal from fibroblasts to macrophages (Figure S4D; Mendeley Figure S4 at https://doi.org/10.17632/kmmw43j2z6.2) with predicted signaling from Fibro_3/4 to Mono_Mac_3/4, specifically through interaction with integrins alpha-V and beta-3 (*Itgav*, *Itgb3*).[68] *Postn* was a top contributing gene to fibroblast factor-10 (Figure S4B), which correlated well in space-time with Mono_Mac factor-22 to make up WH-GM-3 (Figure 4C). Using an *in vitro* stimulation of BMDMs, we confirmed that recombinant POSTN, in combination with plate-bound collagen specifically induced the expression of top contributing members of Mono_Mac factor-22 (e.g., *Gpnmb*, *Pld3*, and *Fabp5*) but not those from other factors (Figure 4G). We then examined if the paired signal and response genes were found co-localized in the healing wound. Imaging sections of day 7 wounds, we were able to simultaneously stain for the protein product of *Postn* (sender) and a response gene in macrophages, *Gpnmb* (Figure S4E). We found GPNMB$^+$ and CD11b$^+$ cells in the vicinity of thick POSTN deposition (Figure S4F). We also observed a gradient in POSTN signal moving outward from the center of the wound, matching our scRNA-seq tile plots as in Figure 3. Concurrently, mean GPNMB signal within CD11b$^+$ cells decreased beyond the original wound edge at around 2 mm distance from the center (Figure S4G), matching the Mono_Mac factor 22 profile (Figure 4B). When examining the distance of CD11b$^+$ cells to the nearest POSTN surface, we also found that GPNMB$^+$CD11b$^+$ cells were significantly closer to POSTN signal than their GPNMB$^-$CD11b$^+$ counterparts, with a median distance of 5 microns vs. 55 microns (Figure S4H).

Extending NMF to all the other cell types, we identified 114 gene programs scattered across our broad cell type definitions (top contributing genes and weights found in Table S1); analysis of their correlated space-time profiles revealed "blocks" of shared space-time patterns including, but also extending beyond, the Early, Edge, Int-In, Late-In, and Late-Ex patterns described above (Figures S4I and S4J; Mendeley Figure S4 at https://doi.org/10.17632/kmmw43j2z6.2).

Identification of conserved gene programs between WH and cancer

The paradigm of the tumor as a wound that never heals has been hypothesized,[28,29] and we sought to quantify the degree the tumor microenvironment (TME) could be described by WH factors.

Figure 4. Gene program analysis identifies modules of gene expression across diverse cell types and predicts cell-cell interactions between macrophages and fibroblasts

(A and B) Schematic showing strategy for NMF-based decomposition of the (A) fibroblast and (B) monocyte/macrophage populations. NMF decomposition of the fibroblast and monocyte/macrophage populations yielded 17/24 factors, respectively. Shown are three example FeaturePlots for factor "expression" and tile plots describing the average loading of the factor as a function of space-time, with colors indicating change of average expression relative to unwounded as in Figure 1I.

(C) Space-time correlation matrix for average factor expression profiles. Correlation was calculated using Pearson correlation and significance adjusted for multiple comparisons using BH correction. +(alpha < 0.05), ++(alpha < 0.005).

(D) Cartoon schematic of hypothetical fibroblast-macrophage crosstalk and progression over the timespan of wound healing. Three putative interactions that we investigate *in vitro* are labeled. WH-GM, wound healing gene movement; OSM, oncostatin M; TNC, tenascin-C; POSTN, periostin; Early-In, early interior; Int-In, intermediate interior; Late-In, late interior.

(E) Real-time quantitative PCR quantification of gene transcripts in PSF's predicted from gene program analysis (see Figure S4B) to contribute most to fibroblast factor-1 as well as genes contributing to other factors as a negative control. Bar chart and color scale denote the $\log_2$ fold-change of relative expression between the OSM treated and untreated PSF's. Error bars denote standard error of the mean from technical triplicates. Data are representative of two independent experiments. Right heatmap shows the normalized gene weight contribution to all 17 identified fibroblast factors for the genes being probed.

(F) Real-time quantitative PCR quantification of gene transcripts in BMDM's predicted from gene program analysis (see Figure S4A) to contribute most to Mono_Mac factor-2 as well as genes contributing to other factors as a negative control. Bar chart and color scale denote the $\log_2$ fold-change of relative expression between the TNC treated and untreated BMDM's. Error bars denote standard error of the mean from technical triplicates. Data are representative of two independent experiments. Right heatmap shows the normalized gene weight contribution to all 17 identified Mono_Mac factors for the genes being probed.

(G) Real-time quantitative PCR quantification of gene transcripts in BMDM's predicted from gene program analysis (see Figure S4A) to contribute most to Mono_Mac factor-22 as well as genes contributing to other factors as a negative control. Bar chart and color scale denote the $\log_2$ fold-change of relative expression between the POSTN treated and untreated BMDM's. Error bars denote standard error of the mean from technical triplicates. Data are representative of two independent experiments. Right heatmap shows the normalized gene weight contribution to all 17 identified Mono_Mac factors for the genes being probed.

See also Figure S4 and Table S2.

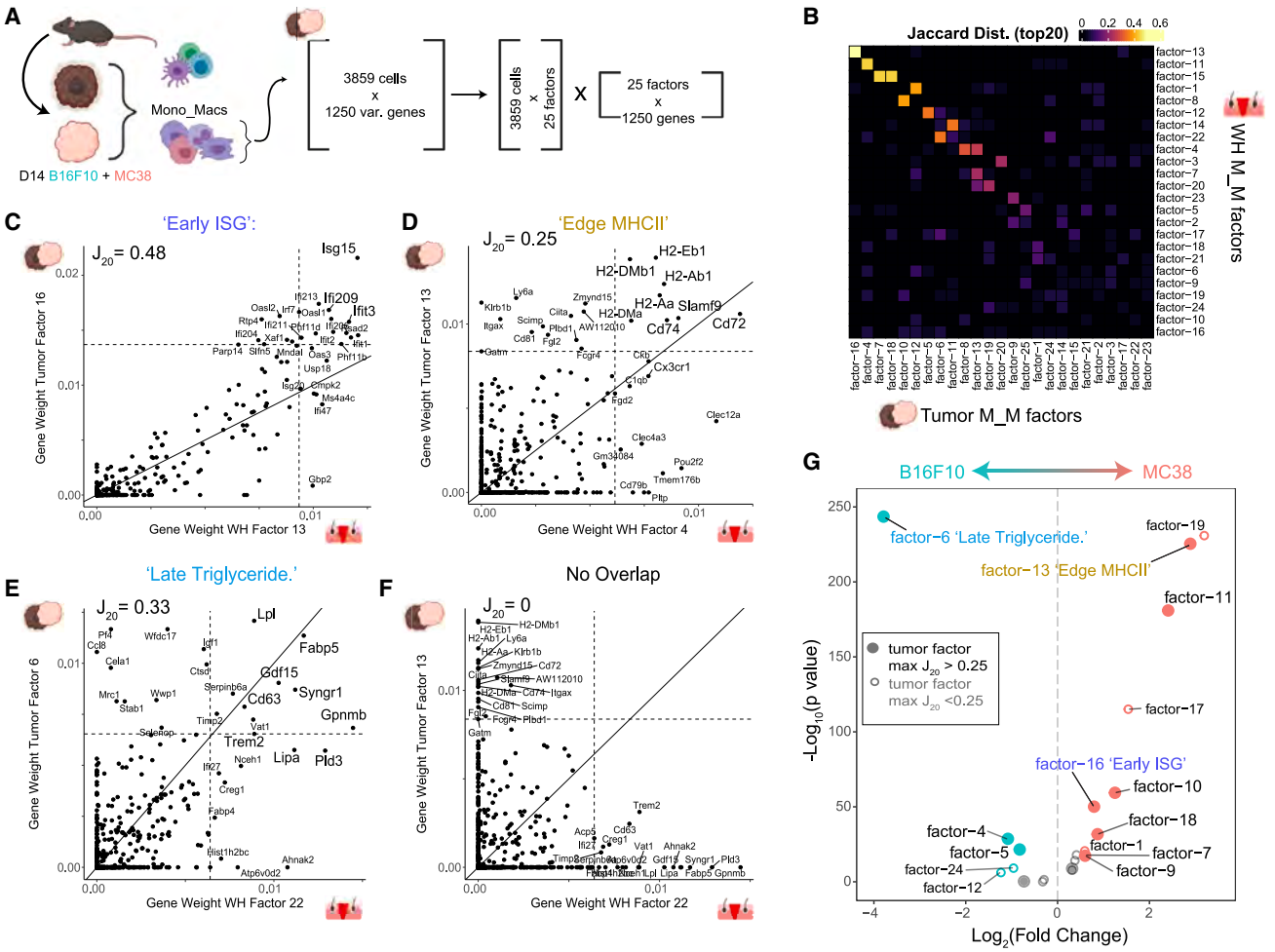

Figure 5. Identification of conserved gene programs in Mono_Mac between wound healing and mouse tumor models

(A) Strategy for generation of a multi-tumor model Mono_Mac CD45$^+$ scRNA-seq dataset. Following integration, Mono_Mac populations were selected for NMF decomposition, starting with 3,859 cells and the top 1,250 variable genes expressed in at least 2% of cells. This resulted in 25 factors of interest based on the cophenetic metric (seen in Figure S5C).

(B) Heatmap showing the Jaccard$_{20}$ distance (defined in STAR Methods) between all 25 Mono_Mac (M_M) tumor and 24 Mono_Mac WH factors based on top contributing gene weights.

(C–F) Scatter plots for selected tumor/WH factor pairs for (C) tumor factor-16 vs. WH factor-13, (D) tumor factor-13 vs. WH factor-4, (E) tumor factor-6 vs. WH factor-22, and (F) tumor factor-13 and WH factor-22 with the gene weight contributions plotted as calculated from the basis matrix in the NMF output (see Figure S4A for WH factors and Figure S5B for tumor factors). Slope represents x = y line and dotted lines represent the weight for the 20th highest gene contribution in either factor. The Jaccard$_{20}$ index is shown and thus reflects the frequency of points in quadrant I over quadrants I, II, and IV. For pairings in (C)–(E), top shared genes in the upper right quadrant were put through Enrichr to find overrepresented cellular processes with the top result by p value listed. Full Enrichr output can be found in the extended data (Table S2).

(G) Volcano plot showing differential loading of factors between MC38 and B16F10 Mono_Mac datasets for the 25 identified factors. y axis denotes log$_{10}$ of unadjusted p value. Labeled points have adjusted p value < 0.05 (Bonferroni correction) and absolute log$_2$ fold-change greater than 0.5. Colored points have absolute log$_2$ fold-change greater than 0.5.

See also Figures S4 and S5.

We hypothesized that NMF analysis could reveal conserved gene programs between the WH and tumor tissue contexts. We first generated an integrated myeloid-subset scRNA-seq dataset from two different mouse tumor models—B16F10 mouse melanoma and MC38 mouse colorectal (Figures 5A and S5A)—and applied our nsNMF workflow, identifying 25 factors (Figures S5B and S5C). We then sought to quantify the degree of factor similarity between the two contexts. We prioritized that a conserved pair of factors exhibit significant overlap in the top contributing genes; therefore, we applied a Jaccard distance metric based on the top 20 genes by weight or Jaccard$_{20}$ (J$_{20}$) distance. Most factor pairings displayed little to no overlap in their top 20 contributing genes, but a few rose prominently from the background (Figure 5B).

We generated scatterplots of gene weights to examine shared gene contributions more closely between pairs of WH and tumor factors (examples in Figures 5C–5F and S5D–S5I). Although most factor pairings resembled Figure 5F with little to no overlap

in gene contributions, we did identify nine strong pairings ($J_{20} > 0.25$) (Figures 5C–5E and S5D–S5I). Gene ontology (GO) analysis on the shared genes in the upper right quadrant revealed unique cellular processes associated with each pairing that could, at least partially, reflect the functional output of those gene programs (full list of GO terms in Table S3). We focus on three of these pairings below:

"Early interferon stimulated gene (ISG)" program: of the stronger pairings, the WH Mono_Mac-13-to-Tumor Mono_Mac-16 factors were highly characterized by a collection of well-described ISGs[69] (Figure 5C). GO analysis yielded the term "type I interferon signaling pathway." In the wound, this WH Mono_Mac factor-13 followed an Early WH-GM1 space-time profile (Figure S4J).

"Edge MHCII program": another factor pairing (WH Mono_Mac-4-to-Tumor Mono_Mac-13; Figure 5D), involved genes associated with antigen presentation through MHCII. In this case, there were highly correlated expression levels of *H2-Ab1*, *H2-Eb1*, and other genes associated with antigen presentation (e.g., *Cd74*). GO analysis indicated antigen processing and presentation via MHCII. WH Mono_Mac factor-4 followed an Edge WH-GM5 space-time profile that seemed to follow the closure of the wound (Figures S4I and S4J).

"Late triglyceride": the WH Mono_Mac factor-22 to tumor Mono_Mac factor-6 pairing was marked by genes including *Gpnmb*, *Fabp5*, *Syngr1*, *Cd63*, *Trem2*, and *Lipa* among others (Figure 5E). GO analysis revealed enrichment for "triglyceride sequestration," suggesting a functional output associated with intracellular vesicle trafficking and exocytosis. This factor also followed the space-time pattern that we termed Late-In or WH-GM3 (Figure S4J).

Finally, we sought to determine whether such programs are used equivalently in the two-model tumor systems. The MC38 dataset displayed significant enrichment of factors including tumor factors 11 and 13, which had a strong ($J_{20} > 0.25$) correspondence to a WH factor. Meanwhile, B16F10 tumors were uniquely marked by a separate and very strong enrichment of factor-6, corresponding to WH factor-22 (Figure 5G). Together, this suggests that although tumors may indeed borrow factors from WH, individual tumors may do so uniquely.

We were also curious as to how different time points of the tumor might resemble different space-time coordinates of WH. We used two published scRNA-seq datasets on fibroblasts collected at different stages of tumor progression in either a B16F10 melanoma model[70] (Figure S5J) or tumors arising in KPP ($Pdx1^{cre/+}$; $LSL{-}Kras^{G12D/+}$; $p16/p19^{flox/flox}$) genetically engineered mouse model (GEMM) animals[54] (Figure S5K). We used our fibroblast factors to generate signature scores for each program in these tumor datasets to relate their similarity to space-time coordinates of WH. Strikingly, we found both tumor models showed similar trajectories over the tumor stage, moving toward the day 7_2 mm and day 7_4 mm coordinates and away from the UW and late edge coordinates (Figures S5L–S5N). This was driven by the gain of factors 8 and 10 and loss of factors 12 and 13, suggesting that as the tumor progresses in these models, the fibroblast compartment comes to resemble a late-resolving wound.

We next sought to generalize our findings to a more clinically relevant setting. Using a merged scRNA-seq dataset collected from patient tumor resections (from lung adenocarcinomas [LUNG] and head and neck squamous cell carcinoma [HNSC]) with some matched adjacent normal tissue (Figure 6A), we extracted the fibroblast and Mono_Mac subsets (Figures 6B, 6D, and S6A–S6D). We applied NMF decomposition and compared gene weight contributions as above, with the conversion of mouse gene symbols to human ones for comparison. Despite the difficulties in comparing gene programs across species and tissue types, we observed several overlapping mouse WH (mWH) and human tumor (HuTumor) factors (Figures S6G and S6H). mWH Mono_Mac factor-22 overlapped well with HuTumor Mono_Mac factor-7 with many overlapping genes as seen in a gene weight scatterplot (Figure 6D). Meanwhile, mWH fibroblast factor-10 was conserved well with HuTumor fibroblast factor-5 (Figure 6E). This suggested that these day 7-dominant gene programs (mWH fibroblast factor-10 and mWH Mono_Mac factor-22) represented a cross-species conserved state in human tissues. When we plotted the mean loading of HuTumor fibro factor-5 vs. the mean loading of HuTumor Mono_Mac factor-7 across samples, we found a correlated increase in these factors going from adjacent normal to tumor tissue in HNSC and LUNG (Figures 6F and 6G). When considering the HNSC and LUNG indications separately, we found a significant correlation between the levels of this HuTumor fibro factor-5 and HuTumor Mono_Mac factor-7. Thus, not only are these factors conserved across species but also their co-occurrence.

Conservation of Mono_Mac factors predicts increased POSTN density and decreased Selectin-P$^+$ vessel density in B16F10 vs. MC38 tumor models

We finally sought to study the conserved gene programs spatially and confirm the differential usage of WH factors in different tumor models. To this end, we used our Mono_Mac factor translation matrix (Figure 5B) and our WH movement identification to make and then test predictions about the state of the tumor microenvironment in either tumor model. As observed in Figure 5G, the Mono_Mac tumor factor-6 was more highly expressed in B16F10 vs. MC38. This tumor macrophage factor corresponded to Mono_Mac WH factor-22 (Figure 5B). We used the observation that the latter factor was paired in a space-time movement with fibroblast factor-10 in our WH dataset (Figure 4C), to form the prediction that the sender signal POSTN, would be more prevalent in B16F10 vs. MC38 model (Figure 7A). Immunofluorescence staining of both tumors identified indeed a profoundly larger density of POSTN fibers within B16F10 tumors compared with MC38 (Figures 7B and 7C). In addition, a considerably larger fraction of CD11b$^+$ cells were in close contact with POSTN fibers in the B16F10 model vs. MC38 (Figures 7D, 7E, and S7A).

Conversely, the shared "Edge MHCII" factor (tumor Mono_Mac factor-13 corresponding to WH Mono_Mac factor-4; Figure 5B) was more dominant in MC38 (Figure 5G). Going back to the space-time correlations in Figure S4J, WH Mono_Mac factor-4, as an Edge pattern WH-GM5, grouped with WH endothelial factor-8, which comprised genes including *Selp*, *Vwf*, and *Ackr1*. Following a similar line of inference as before with POSTN signaling to macrophages, we predicted a higher density of Selectin-P$^+$ vasculature in MC38 vs. B16F10 tumors (Figure 7F).

Using 3D imaging of cleared thick tumor sections (250 μm) (Figures 7G and S7B), we found a markedly increased density

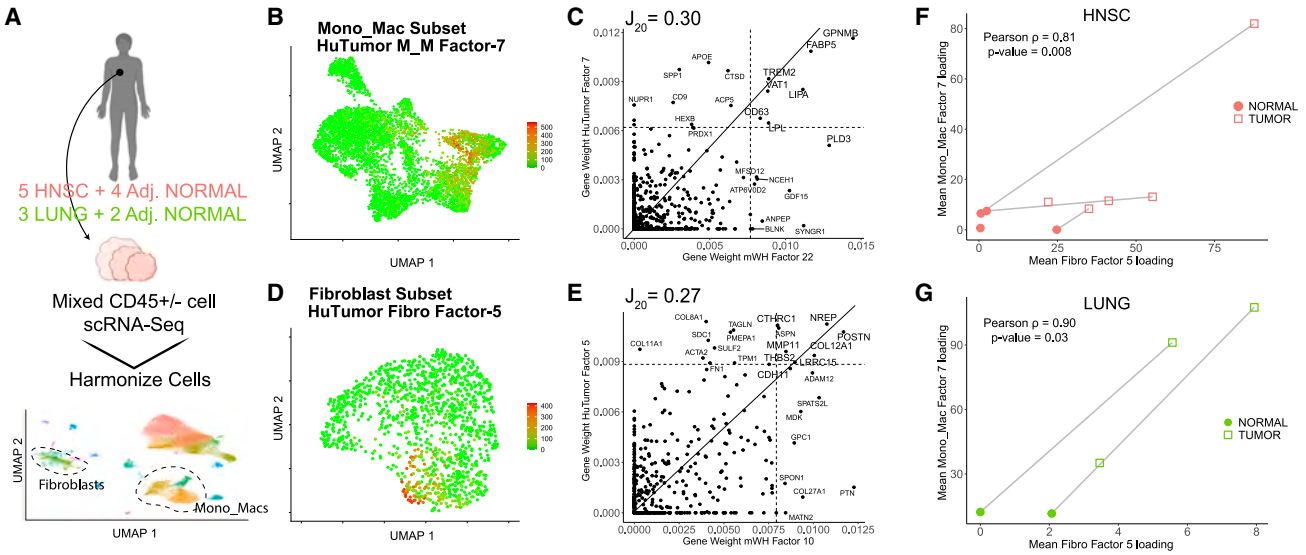

Figure 6. The wound healing gene movement-3 (WH-GM3) is conserved in human tumors

(A) scRNA-seq datasets of both CD45$^+$ and CD45$^-$ compartments from patient tumor resections and adjacent normal samples were collected from lung adenocarcinomas (LUNG) and head and neck squamous cell carcinomas (HNSC) as described in STAR Methods (n = 77,270 cells).

(B) Feature plot shown for the Mono_Mac object for HuTumor Mono_Mac factor-7.

(C) Scatter plot for gene weights from factor pair (human) HuTumor Mono_Mac factor-7 vs. (mouse) mWH Mono_Mac factor-22 (right). Mouse gene symbols were converted to their ortholog for comparison purposes with the gene weight contributions plotted as calculated from the basis matrix in the NMF output. Slope represents x = y line, and dotted lines represent the weight for the 20th highest gene contribution in either factor. The Jaccard$_{20}$ index is shown.

(D) Feature plot shown for the fibroblast object for HuTumor fibro factor-5.

(E) Scatter plots for selected human (hu) tumor/murine (m) WH factor pairs huTumor Fibroblast Factor 5 vs. mouse WH Fibroblast factor-10. Mouse gene symbols were converted to their ortholog for comparison purposes with the gene weight contributions plotted as calculated from the basis matrix in the NMF output. Slope represents x = y line and dotted lines represent the weight for the 20th highest gene contribution in either factor. The Jaccard$_{20}$ index is shown.

(F and G) Scatter plot showing mean factor levels calculated for huTumor Mono_Mac factor-7 and huTumor fibroblast factor-5 across HNSC samples (F) and LUNG (G). Point shapes denote adjacent normal vs. tumor samples and lines between points represent paired adjacent normal and tumor samples. Pearson's rho denoted and p value calculated via Pearson's method.

See also Figure S6 and Table S3.

of Selectin-P$^+$ vasculature in the MC38 tumor relative to B16F10 tumor (Figure 7H), consistent with our prediction in Figure 7F. Analysis also revealed clear physical proximity of MHCII$^+$ cells (cyan points) with Selectin-P$^+$ vasculature (green) vs. Selectin-P$^-$ vasculature (red) in both tumor models (Figures 7I, 7J, and S7C). We also note this preference for Selectin-P vessels was not found in MHCII$^-$ cells (Figures 7J and S7C). These lines of evidence provide examples of how the conceptual framework of conserved gene programs and multicellular movements can inform hypothesis generation-spanning tissue contexts.

DISCUSSION

Characterizing how diverse cell types are spatially and temporally organized within the tissue will help us understand the underlying dynamic nature of tissues. Here, we established a spatiotemporal framework to study pairing of cell types during the physiologically complex process of wound repair. In this setting, the concept that spatiotemporal correlation may indicate paired biology drove the identification of groups of cell types and gene programs that together form larger cellular movements and are partially conserved in both skin repair and tumor growth.

Several fibroblast-macrophage interactions have been described in health and disease, such as fibrosis and cancer.[22] The use of STCA takes this systematically one step further and identified three distinct fibroblast-macrophage cellular pairings during wound repair (Figure 3J), each characterized by a distinct space-time pattern during the repair process. The earliest pattern consisted of inflammatory Fibro_1, expressing the neutrophil-attracting chemokine *Cxcl5*[71] and the early inflammatory gene *Ptx3*.[72] Accordingly, this early pattern was accompanied by neutrophils and monocytes (Figure S3K) whose accumulation in early wounds had been previously identified[3] but not tied to this fibroblast population. Conversely, the Late-Ex pattern ties together Fibro_5, mast cells, MHCII^{hi} Mono_Mac, T cells, and keratinocyte subsets. These multicellular patterns are akin to the described collection of cell types that coordinate monocyte differentiation in the liver.[6]

By combining NMF-based decomposition with spatiotemporal data, we identified co-occurring gene programs that provide candidates for reciprocal interaction between cell types. We present this approach as a framework for identifying CCC pathways and their downstream effects on gene expression. In our framework, factors or gene programs represent a functional module activated in a cell type due to response to external stimuli, which, in turn, may be derived from programs activated in other cell types. One example is OSM from Mono_Mac to fibroblasts, previously known to induce *Serpine1* and *Il33* upregulation.[73,74] Using NMF analysis combined with spatiotemporal

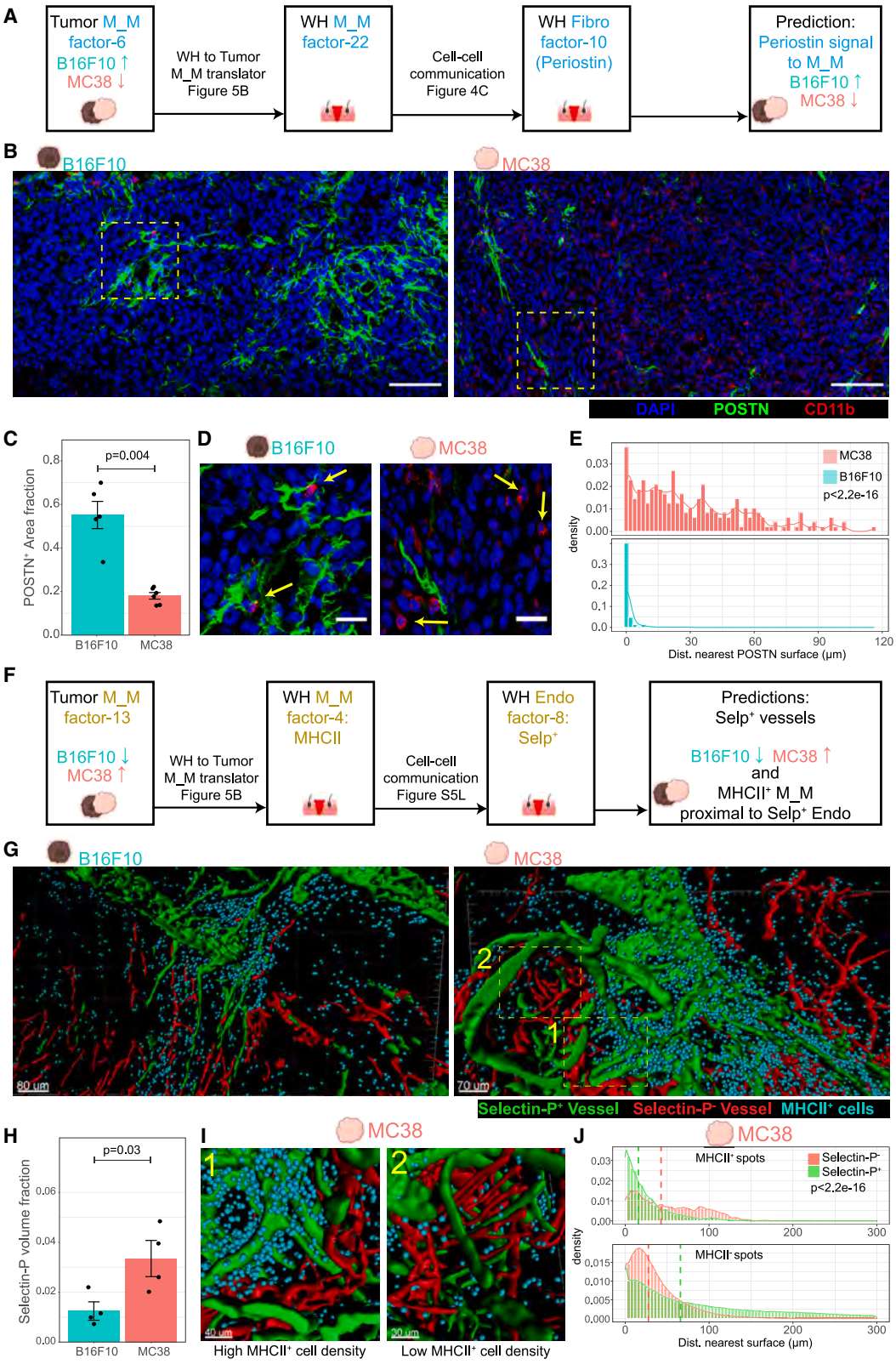

Figure 7. Conservation of Mono_Mac factors predicts specific differential features of microenvironments in B16F10 vs. MC38 tumor models

(A) Schematic for hypothesis generation in the tumor setting. Translation of the tumor Mono_Mac (M_M) factor-6 to the WH Mono_Mac factor-22 allows prediction that the same stimuli (POSTN from WH fibro factor-10) might underlie tumor Mono_Mac factor-6 and thus be more prevalent in the B16F10 vs. MC38 tumor model.

(legend continued on next page)

correlations across cell types, we identified a host of other genes (e.g., *Glul*, *Mt2*, and *Acsl4*) (Figure 4E) not previously described to be OSM induced.

Reciprocally, we predicted TNC to induce a host of genes (e.g., *Cd83*, *Ccrl2*, and *Id3*) in Mono_Mac factor-2 in the day 3 wound interior. Testing TNC treatment on BMDMs revealed a specific upregulation of these predicted genes in a specific manner, failing to upregulate genes contributing to other gene programs (Figure 4F). Recent work has discovered a TNC-(Toll-like receptor 4) TLR4 signaling axis in macrophages that promotes a pro-metastatic perivascular niche[67]; we note that several of these target genes we verified are known to sit downstream of TLR4 activation.[75,76]

Similarly, our movement identification suggested POSTN, which emerges later in WH in fibroblasts, as a candidate to induce the genes defined in factor-22 in Mono_Mac's (Figure 4G) in day 7 wound interiors. This factor includes *Gpnmb*, *Lipa*, and *Trem2*, implicated as a marker for a tumor-associated macrophage population that can be targeted for immunotherapy.[77–79] Previous reports have mainly described the ability of POSTN to promote adhesion and migration of macrophages in tumor settings.[77–82]

Our dataset suggests a multitude of major groupings of spatiotemporally correlated gene programs in disparate cell types, with each grouping displaying a unique space-time pattern (Figures S4I and S4J; Mendeley Figure S4 at https://doi.org/10.17632/kmmw43j2z6.2). Similar to the idea of ''hubs'' of gene programs, these movements of gene programs could represent spatially co-localized, functional units of cell organization in tissue.[62] Additionally, such groupings could underlie the findings that tumor microenvironments tend to adopt defined compositional ''archetypes.''[83] The gene programs identified here, and their shared spatiotemporal profiles, will inform future studies to identify which correlations are indicative of true CCC.[12,84]

We posit that gene program analysis can serve as a powerful tool for integrative studies across tissue types and disease models.[33] We identified conserved gene programs in the Mono_Mac populations from two tumor models and our WH dataset. We also found conserved gene programs in both macrophages and fibroblasts from human tumor samples, demonstrating that these programs may represent fundamental cross-species biology (Figures 6A–6E). We also note that factor pairings are not perfect, with some genes showing little contribution in one setting vs. major contribution in another (Figure 5B). We theorize that this could indicate either a purely coincidental co-expression in one setting, gene dropout differences, or an additional layer of epigenetic regulation. We also note the presence of many factors without a good counterpart that could represent artifacts introduced in the processing pipeline or be representative of context-specific programs. This methodology could also be applied to models of fibrosis,[85] wherein many of the same CCCs that drive regeneration become dysregulated, e.g., persisting inappropriately.[22,86–88] Thus, identifying the space-time profiles of conserved gene programs and between fibrosis, WH, and tumorigenesis could identify where the dynamics of pathologies begin to diverge in state space from normal.[29]

We further demonstrated that testable hypotheses can be generated from our correlative studies by proceeding in a two-step fashion, first translating tumor Mono_Mac factors to WH Mono_Mac factors (Figure 5B), then using identified multicellular movements to translate WH Mono_Mac factors to correlated WH factors in other cell types (Figure S4J). This analysis allowed us to predict increased POSTN signaling to macrophages in B16F10 vs. MC38 tumors that we verified downstream (Figures 7A–7E). Of note, this pair of macrophage/fibroblast programs (Mono_Mac factor-22 and fibroblast factor-10) that dominated in the day 7 wound interior was found conserved in human tumor samples from HNSC and lung adenocarcinoma resections (Figures 6A–6E) with a paired enrichment in tumor tissue vs. adjacent normal (Figures 6F and 6G). We suggest that different tumor archetypes in human and mouse models can be described in terms of WH space-time coordinates; in this instance, the B16F10 model and some human tumors can be said to resemble a day 7 wound interior in the resolution phase. Altogether, our in-silico analysis suggests that as tumors progress, they become enriched in features found in the late wound interior while losing features associated with the UW and late wound exterior coordinates

(B) Representative immunofluorescent images of 10 μm sections of day 14 B16F10 and MC38 tumors stained for DAPI (blue), POSTN (green), and CD11b (red). Scale bars, 100 μm. Representative of 2 independent replicates consisting of total of 6 and 5 samples for MC38 and B16F10, respectively.

(C) Barchart denoting fraction area of POSTN$^+$ surfaces as a fraction of the total imaged tissue area. One-sided Wilcoxon rank-sum test used. Each point represents a scanned area from 6/5 separate tumor samples MC38/B16F10 respectively.

(D) Insets from denoted regions of interest in Figure 6B. Arrows denote CD11b$^+$ cells in close contact with POSTN$^+$ surfaces (B16F10) or not (MC38). Scale bars, 25 μm.

(E) Histograms showing distribution of distance of CD11b$^+$ cells to nearest POSTN surface. Representative of 3 independent replicates (3 tumors). Bin-width = 2 μm. p value calculated via Kolmogorov-Smirnov (KS) test for distribution similarity.

(F) Schematic for hypothesis generation in the tumor setting. Translation of the tumor Mono_Mac factor-13 to the WH Mono_Mac factor-4 allows prediction that the same association between WH Mono_Mac factor-4 with endothelial WH factor-8 might be found in the tumor setting and that endothelial factor-8 might be more prevalent in MC38 vs. B16F10 tumor model.

(G) Processed 3D images of cleared 250 μm thick tumor slices from a (left) B16F10 and (right) MC38 tumor. Generated surfaces based on Selectin-P$^+$ staining (green) and CD31$^+$/Selectin-P$^-$ signal (red). Dots (cyan) denote MHCII$^+$ cells. Representative of 4 independent replicates (4 separate tumors). Scale bars, 80 and 70 microns in B16F10 and MC38 images, respectively.

(H) Bar chart showing comparison of the cumulative Selectin-P$^+$ surfaces volume normalized to the total imaged tissue volume between MC38 and B16F10. One-sided Wilcoxon rank-sum test used for significance testing.

(I) Zoomed in and rotated insets from MC38 tumor in Figure 6G exemplifying (1) dense accumulation of MHCII$^+$ cells proximal to Selectin-P$^+$ vessels and (2) sparse MHCII$^+$ cell accumulation proximal to Selectin-P$^-$. Scale bars, 40 and 30 microns, respectively.

(J) Histograms indicating the distances of MHCII$^+$ spots and MHCII$^-$ spots to the nearest Selectin-P$^+$ or Selectin-P$^-$ surface in the MC38 model. Dashed line indicates the median. Histograms representative of 4 independent replicates (4 separate tumors). p value calculated via KS test for distribution similarity.
See also Figure S7.

(Figures S5L–S5N). Notably, our tumor datasets lack spatial resolution, and future work could illuminate neighborhoods in the tumor microenvironment with similarity to distinct wound space-time points using spatial transcriptomics.[89–91] Conversely, we also predicted an enrichment for P-selectin-expressing endothelial cells (endo factor-8) in MC38 vs. B16F10 tumors (Figure 7F). The close association of MHCII^{hi} macrophages with CD31^{+} vasculature has been reported previously[92] but not specifically with Selectin-P^{+} vasculature. Of interest, the endothelial factor-8 genes including *Selp*, *Sele*, and *Ackr1* also define a tumor-associated high endothelial venule network found to be correlated with patient response to checkpoint blockade immunotherapy,[93] suggesting an etiology for the unresponsiveness of the B16-F10 melanoma model vs. the MC38 model to ICB.[94]

Limitations of the study

Our scRNA-seq study identified several immune and non-immune cells and their dynamic changes during the skin repair process. However, we noticed no capture of adipocytes, neurons, or glial cells. Presumably, our workflow of cell sorting and 10× Genomics encapsulation led to their disproportionate loss. This precludes analysis of their potential involvement in the movements we describe. In addition, we noted a reduced representation of neutrophils in our scRNA-seq study compared with our initial CyTOF study, possibly due to the sensitivity of these cells to the scRNA-seq workflow. Previous studies have highlighted the importance of adipocytes in skin repair,[34] as well as the role of macrophage-neuron crosstalk skin homeostasis.[95]

Although we show multiple lines of evidence for POSTN-mediated factor-22 upregulation in macrophages, several questions remain. First, POSTN is known to mediate several effects on TGFβ signaling[96] and macrophage recruitment.[97] The signaling events leading directly from POSTN binding via theoretical receptors (ITGAV, ITGAM) to upregulation of Mono_Mac factor-22 genes remain unclear. Second, in our tumor settings, it remains unknown if the POSTN observed is derived from fibroblasts or tumor cells themselves.

The skin is colonized by a microbiome that breaches the skin barrier on injuries that are sensed by local immune cells. In our otherwise sterile tumor models, pathogen sensing would be less likely to influence CCC. Thus, commonalities discovered here using subcutaneous tumor models and skin wounding are conserved in both the absence and presence of pathogen detection, whereas programs during WH without a counterpart in tumor models may represent a response downstream of pathogen sensing.

STAR★METHODS

Detailed methods are provided in the online version of this paper and include the following:

- KEY RESOURCES TABLE
- RESOURCE AVAILABILITY
  - Lead contact
  - Materials availability
  - Data and code availability
- EXPERIMENTAL MODEL AND STUDY PARTICIPANT DETAILS
  - Animals
  - Cell lines
  - Human tumor collection of the UCSF Immunoprofiler Initiative (IPI)
  - Human tissue digestion and cell sorting for single cell RNA sequencing analysis
- METHOD DETAILS
  - Full-thickness wounding
  - Tissue Processing
  - Mass Cytometry
  - Single cell RNA sequencing of skin wound-associated cells
  - Candidate identification of ligand-receptor interactions using CellChat
  - Embedding a low-dimensional representation of samples using PhEMD
  - Pseudotime Analysis in scRNAseq data set
  - Ce3D Tissue Clearing and Whole Mount Imaging
  - Ex vivo experiments of primary skin fibroblast and bone marrow-derived macrophages (BMDMs)
- QUANTIFICATION AND STATISTICAL ANALYSIS
  - Quantification of cells in microscopy images
  - Space/Time Tileplot of cell frequencies
  - Space/Time Correlation Analysis (STCA)
  - NMF Decomposition

SUPPLEMENTAL INFORMATION

Supplemental information can be found online at https://doi.org/10.1016/j.stem.2023.05.001.

ACKNOWLEDGMENTS

We would like to thank Drs. Hong-Erh Liang and Richard Locksley for the generous gift of the Arg1-reporter mouse. We also thank Drs. Chris McGinnis and Zev Gartner for the lipid-modified oligonucleotides (LMOs) and comments on the manuscript and Dr. Ian Boothby for advice on the mWH model. Additionally, we thank members of the Krummel lab for comments on the manuscript. This work was supported by funds from NIH R01CA197363. K.H.H. is supported by the American Cancer Society Postdoctoral Fellowship (#133078-PF-19-222-01-LIB) and N.F.K. is supported by NIH T32 5T32CA108462-17. Flow cytometry was performed at the UCSF Parnassus Flow CoLab, RRID:SCR_018206, and supported in part by the DRC Center Grant NIH P30 DK063720. We also thank the Data Science CoLab for bioinformatic support and the Center for Advanced Technology at UCSF for sequencing support. Finally, we thank all patients and their families for placing their trust in us.

AUTHOR CONTRIBUTIONS

Conceptualization, K.H.H., N.F.K., and M.F.K.; methodology, K.H.H. and N.F.K.; investigation, K.H.H., N.F.K., and T.C.; human sample acquisition, J.T., P.H., and J.R.K.; supervision of human sample acquisition, A.J.C.; formal analysis, K.H.H., N.F.K., T.C., and B.S.; writing – original draft, K.H.H. and N.F.K.; writing – review & editing, K.H.H., N.F.K., P.H., J.R.K., A.J.C., T.C., and M.F.K.; funding acquisition, M.F.K.; resources, M.F.K.; supervision, M.F.K. and K.H.H.

DECLARATION OF INTERESTS

M.F.K. is a founder and shareholder of PIONYR immunotherapeutic and FOUNDERY innovations.

Received: May 25, 2022
Revised: March 13, 2023
Accepted: May 2, 2023
Published: June 1, 2023

REFERENCES

1. Wertheimer, T., Velardi, E., Tsai, J., Cooper, K., Xiao, S., Kloss, C.C., Ottmüller, K.J., Mokhtari, Z., Brede, C., deRoos, P., et al. (2018). Production of BMP4 by endothelial cells is crucial for endogenous thymic regeneration. Sci. Immunol. *3*, eaal2736. https://doi.org/10.1126/sciimmunol.aal2736.
2. Walesky, C.M., Kolb, K.E., Winston, C.L., Henderson, J., Kruft, B., Fleming, I., Ko, S., Monga, S.P., Mueller, F., Apte, U., et al. (2020). Functional compensation precedes recovery of tissue mass following acute liver injury. Nat. Commun. *11*, 5785. https://doi.org/10.1038/s41467-020-19558-3.
3. Rodrigues, M., Kosaric, N., Bonham, C.A., and Gurtner, G.C. (2019). Wound healing: A cellular perspective. Physiol. Rev. *99*, 665–706. https://doi.org/10.1152/physrev.00067.2017.
4. Li, P., and Elowitz, M.B. (2019). Communication codes in developmental signaling pathways. Development *146*, dev170977. https://doi.org/10.1242/dev.170977.
5. Zhou, X., Franklin, R.A., Adler, M., Jacox, J.B., Bailis, W., Shyer, J.A., Flavell, R.A., Mayo, A., Alon, U., and Medzhitov, R. (2018). Circuit design features of a stable two-cell system. Cell *172*, 744–757.e17. https://doi.org/10.1016/j.cell.2018.01.015.
6. Bonnardel, J., T'Jonck, W., Gaublomme, D., Browaeys, R., Scott, C.L., Martens, L., Vanneste, B., De Prijck, S., Nedospasov, S.A., Kremer, A., et al. (2019). Stellate cells, hepatocytes, and endothelial cells imprint the Kupffer cell identity on monocytes colonizing the liver macrophage niche. Immunity *51*, 638–654.e9. https://doi.org/10.1016/j.immuni.2019.08.017.
7. Satija, R., Farrell, J.A., Gennert, D., Schier, A.F., and Regev, A. (2015). Spatial reconstruction of single-cell gene expression data. Nat. Biotechnol. *33*, 495–502. https://doi.org/10.1038/nbt.3192.
8. Jin, W., Tang, Q., Wan, M., Cui, K., Zhang, Y., Ren, G., Ni, B., Sklar, J., Przytycka, T.M., Childs, R., et al. (2015). Genome-wide detection of DNase I hypersensitive sites in single cells and FFPE tissue samples. Nature *528*, 142–146. https://doi.org/10.1038/nature15740.
9. Buenrostro, J.D., Wu, B., Litzenburger, U.M., Ruff, D., Gonzales, M.L., Snyder, M.P., Chang, H.Y., and Greenleaf, W.J. (2015). Single-cell chromatin accessibility reveals principles of regulatory variation. Nature *523*, 486–490. https://doi.org/10.1038/nature14590.
10. Jin, S., Guerrero-Juarez, C.F., Zhang, L., Chang, I., Ramos, R., Kuan, C.H., Myung, P., Plikus, M.V., and Nie, Q. (2021). Inference and analysis of cell-cell communication using CellChat. Nat. Commun. *12*, 1088. https://doi.org/10.1038/s41467-021-21246-9.
11. Efremova, M., Vento-Tormo, M., Teichmann, S.A., and Vento-Tormo, R. (2020). CellPhoneDB: inferring cell–cell communication from combined expression of multi-subunit ligand–receptor complexes. Nat. Protoc. *15*, 1484–1506. https://doi.org/10.1038/s41596-020-0292-x.
12. Browaeys, R., Saelens, W., and Saeys, Y. (2020). NicheNet: modeling intercellular communication by linking ligands to target genes. Nat. Methods *17*, 159–162. https://doi.org/10.1038/s41592-019-0667-5.
13. Moor, A.E., Harnik, Y., Ben-Moshe, S., Massasa, E.E., Rozenberg, M., Eilam, R., Bahar Halpern, K., and Itzkovitz, S. (2018). Spatial reconstruction of single enterocytes uncovers broad zonation along the intestinal villus axis. Cell *175*, 1156–1167.e15. https://doi.org/10.1016/j.cell.2018.08.063.
14. Manco, R., Averbukh, I., Porat, Z., Bahar Halpern, K., Amit, I., and Itzkovitz, S. (2021). Clump sequencing exposes the spatial expression programs of intestinal secretory cells. Nat. Commun. *12*, 3074. https://doi.org/10.1038/s41467-021-23245-2.
15. Egozi, A., Bahar Halpern, K., Farack, L., Rotem, H., and Itzkovitz, S. (2020). Zonation of pancreatic acinar cells in diabetic mice. Cell Rep. *32*, 108043. https://doi.org/10.1016/j.celrep.2020.108043.
16. Droin, C., Kholtei, J.E., Bahar Halpern, K., Hurni, C., Rozenberg, M., Muvkadi, S., Itzkovitz, S., and Naef, F. (2021). Space-time logic of liver gene expression at sub-lobular scale. Nat. Metab. *3*, 43–58. https://doi.org/10.1038/s42255-020-00323-1.
17. Martin, P. (1997). Wound healing - Aiming for perfect skin regeneration. Science *276*, 75–81. https://doi.org/10.1126/science.276.5309.75.
18. Eming, S.A., Wynn, T.A., and Martin, P. (2017). Inflammation and metabolism in tissue repair and regeneration. Science *356*, 1026–1030. https://doi.org/10.1126/science.aam7928.
19. Brazil, J.C., Quiros, M., Nusrat, A., and Parkos, C.A. (2019). Innate immune cell–epithelial crosstalk during wound repair. J. Clin. Invest. *129*, 2983–2993. https://doi.org/10.1172/JCI124618.
20. Eming, S.A., Martin, P., and Tomic-Canic, M. (2014). Wound repair and regeneration: mechanisms, signaling, and translation. Sci. Transl. Med. *6*, 265sr6. https://doi.org/10.1126/scitranslmed.3009337.
21. Wilkinson, H.N., and Hardman, M.J. (2020). Wound healing: cellular mechanisms and pathological outcomes. Open Biol. *10*, 200223. https://doi.org/10.1098/rsob.200223.
22. Buechler, M.B., Fu, W., and Turley, S.J. (2021). Fibroblast-macrophage reciprocal interactions in health, fibrosis, and cancer. Immunity *54*, 903–915. https://doi.org/10.1016/j.immuni.2021.04.021.
23. Lucas, T., Waisman, A., Ranjan, R., Roes, J., Krieg, T., Müller, W., Roers, A., and Eming, S.A. (2010). Differential roles of macrophages in diverse phases of skin repair. J. Immunol. *184*, 3964–3977. https://doi.org/10.4049/jimmunol.0903356.
24. Shook, B.A., Wasko, R.R., Rivera-Gonzalez, G.C., Salazar-Gatzimas, E., López-Giráldez, F., Dash, B.C., Muñoz-Rojas, A.R., Aultman, K.D., Zwick, R.K., Lei, V., et al. (2018). Myofibroblast proliferation and heterogeneity are supported by macrophages during skin repair. Science *362*. https://doi.org/10.1126/science.aar2971.
25. Liu, S.X., Gustafson, H.H., Jackson, D.L., Pun, S.H., and Trapnell, C. (2020). Trajectory analysis quantifies transcriptional plasticity during macrophage polarization. Sci. Rep. *10*, 12273. https://doi.org/10.1038/s41598-020-68766-w.
26. Guerrero-Juarez, C.F., Dedhia, P.H., Jin, S., Ruiz-Vega, R., Ma, D., Liu, Y., Yamaga, K., Shestova, O., Gay, D.L., Yang, Z., et al. (2019). Single-cell analysis reveals fibroblast heterogeneity and myeloid-derived adipocyte progenitors in murine skin wounds. Nat. Commun. *10*, 650. https://doi.org/10.1038/s41467-018-08247-x.
27. Brancato, S.K., and Albina, J.E. (2011). Wound macrophages as key regulators of repair: origin, phenotype, and function. Am. J. Pathol. *178*, 19–25. https://doi.org/10.1016/j.ajpath.2010.08.003.
28. Dvorak, H.F. (2015). Tumors: wounds that do not heal-redux. Cancer Immunol. Res. *3*, 1–11. https://doi.org/10.1158/2326-6066.CIR-14-0209.
29. MacCarthy-Morrogh, L., and Martin, P. (2020). The hallmarks of cancer are also the hallmarks of wound healing. Sci. Signal. *13*, eaay8690. https://doi.org/10.1126/SCISIGNAL.AAY8690.
30. Nathan, C., and Ding, A. (2010). Nonresolving inflammation. Cell *140*, 871–882. https://doi.org/10.1016/j.cell.2010.02.029.
31. Rosato, P.C., Wijeyesinghe, S., Stolley, J.M., and Masopust, D. (2020). Integrating resident memory into T cell differentiation models. Curr. Opin. Immunol. *63*, 35–42. https://doi.org/10.1016/j.coi.2020.01.001.
32. Lavin, Y., Winter, D., Blecher-Gonen, R., David, E., Keren-Shaul, H., Merad, M., Jung, S., and Amit, I. (2014). Tissue-resident macrophage enhancer landscapes are shaped by the local microenvironment. Cell *159*, 1312–1326. https://doi.org/10.1016/j.cell.2014.11.018.
33. Kinker, G.S., Greenwald, A.C., Tal, R., Orlova, Z., Cuoco, M.S., McFarland, J.M., Warren, A., Rodman, C., Roth, J.A., Bender, S.A., et al. (2020). Pan-cancer single-cell RNA-seq identifies recurring programs of cellular heterogeneity. Nat. Genet. *52*, 1208–1218. https://doi.org/10.1038/s41588-020-00726-6.
34. Shook, B.A., Wasko, R.R., Mano, O., Rutenberg-Schoenberg, M., Rudolph, M.C., Zirak, B., Rivera-Gonzalez, G.C., López-Giráldez, F., Zarini, S., Rezza, A., et al. (2020). Dermal adipocyte lipolysis and

myofibroblast conversion are required for efficient skin repair. Cell Stem Cell *26*, 880–895.e6. https://doi.org/10.1016/j.stem.2020.03.013.

35. Driskell, R.R., Lichtenberger, B.M., Hoste, E., Kretzschmar, K., Simons, B.D., Charalambous, M., Ferron, S.R., Herault, Y., Pavlovic, G., Ferguson-Smith, A.C., et al. (2013). Distinct fibroblast lineages determine dermal architecture in skin development and repair. Nature *504*, 277–281. https://doi.org/10.1038/nature12783.
36. Mascharak, S., des Jardins-Park, H.E., Davitt, M.F., Griffin, M., Borrelli, M.R., Moore, A.L., Chen, K., Duoto, B., Chinta, M., Foster, D.S., et al. (2021). Preventing Engrailed-1 activation in fibroblasts yields wound regeneration without scarring. Science *372*, eaba2374. https://doi.org/10.1126/science.aba2374.
37. McGinnis, C.S., Patterson, D.M., Winkler, J., Conrad, D.N., Hein, M.Y., Srivastava, V., Hu, J.L., Murrow, L.M., Weissman, J.S., Werb, Z., et al. (2019). MULTI-seq: sample multiplexing for single-cell RNA sequencing using lipid-tagged indices. Nat. Methods *16*, 619–626. https://doi.org/10.1038/s41592-019-0433-8.
38. Menezes, S., Melandri, D., Anselmi, G., Perchet, T., Loschko, J., Dubrot, J., Patel, R., Gautier, E.L., Hugues, S., Longhi, M.P., et al. (2016). The heterogeneity of Ly6Chi monocytes controls their differentiation into iNOS+ macrophages or monocyte-derived dendritic cells. Immunity *45*, 1205–1218. https://doi.org/10.1016/j.immuni.2016.12.001.
39. Boulet, S., Daudelin, J.F., Odagiu, L., Pelletier, A.N., Yun, T.J., Lesage, S., Cheong, C., and Labrecque, N. (2019). The orphan nuclear receptor NR4A3 controls the differentiation of monocyte-derived dendritic cells following microbial stimulation. Proc. Natl. Acad. Sci. USA *116*, 15150–15159. https://doi.org/10.1073/pnas.1821296116.
40. Das, H., Kumar, A., Lin, Z., Patino, W.D., Hwang, P.M., Feinberg, M.W., Majumder, P.K., and Jain, M.K. (2006). Kruppel-like factor 2 (KLF2) regulates proinflammatory activation of monocytes. Proc. Natl. Acad. Sci. USA *103*, 6653–6658. https://doi.org/10.1073/pnas.0508235103.
41. Bennett, F.C., Bennett, M.L., Yaqoob, F., Mulinyawe, S.B., Grant, G.A., Hayden Gephart, M., Plowey, E.D., and Barres, B.A. (2018). A combination of ontogeny and CNS environment establishes microglial identity. Neuron *98*, 1170–1183.e8. https://doi.org/10.1016/j.neuron.2018.05.014.
42. Hammond, T.R., Dufort, C., Dissing-Olesen, L., Giera, S., Young, A., Wysoker, A., Walker, A.J., Gergits, F., Segel, M., Nemesh, J., et al. (2019). Single-cell RNA sequencing of microglia throughout the mouse lifespan and in the injured brain reveals complex cell-state changes. Immunity *50*, 253–271.e6. https://doi.org/10.1016/j.immuni.2018.11.004.
43. Trapnell, C., Cacchiarelli, D., Grimsby, J., Pokharel, P., Li, S., Morse, M., Lennon, N.J., Livak, K.J., Mikkelsen, T.S., and Rinn, J.L. (2014). The dynamics and regulators of cell fate decisions are revealed by pseudotemporal ordering of single cells. Nat. Biotechnol. *32*, 381–386. https://doi.org/10.1038/nbt.2859.
44. Blecher-Gonen, R., Bost, P., Hilligan, K.L., David, E., Salame, T.M., Roussel, E., Connor, L.M., Mayer, J.U., Bahar Halpern, K., Tóth, B., et al. (2019). Single-cell analysis of diverse pathogen responses defines a molecular roadmap for generating antigen-specific immunity. Cell Syst. *8*, 109–121.e6. https://doi.org/10.1016/j.cels.2019.01.001.
45. Dean, R.A., Cox, J.H., Bellac, C.L., Doucet, A., Starr, A.E., and Overall, C.M. (2008). Macrophage-specific metalloelastase (MMP-12) truncates and inactivates ELR + CXC chemokines and generates CCL2, -7, -8, and -13 antagonists: Potential role of the macrophage in terminating polymorphonuclear leukocyte influx. Blood *112*, 3455–3464. https://doi.org/10.1182/blood-2007-12-129080.
46. Li, W., Germain, R.N., and Gerner, M.Y. (2019). High-dimensional cell-level analysis of tissues with Ce3D multiplex volume imaging. Nat. Protoc. *14*, 1708–1733. https://doi.org/10.1038/s41596-019-0156-4.
47. Jablonski, K.A., Amici, S.A., Webb, L.M., Ruiz-Rosado, J.D.D., Popovich, P.G., Partida-Sanchez, S., and Guerau-De-Arellano, M. (2015). Novel markers to delineate murine M1 and M2 macrophages. PLoS One *10*, e0145342. https://doi.org/10.1371/journal.pone.0145342.
48. Mujal, A.M., Combes, A.J., Rao, A.A., Binnewies, M., Samad, B., Tsui, J., Boissonnas, A., Pollack, J.L., Argüello, R.J., Meng, M.V., et al. (2022). Holistic characterization of tumor monocyte-to-macrophage differentiation integrates distinct immune phenotypes in kidney cancer. Cancer Immunol. Res. *10*, 403–419. https://doi.org/10.1158/2326-6066.CIR-21-0588.
49. Schneider, C., Lee, J., Koga, S., Ricardo-Gonzalez, R.R., Nussbaum, J.C., Smith, L.K., Villeda, S.A., Liang, H.E., and Locksley, R.M. (2019). Tissue-resident Group 2 innate lymphoid cells differentiate by layered ontogeny and in situ perinatal priming. Immunity *50*, 1425–1438.e5. https://doi.org/10.1016/j.immuni.2019.04.019.
50. Yu, H., Yoo, P.K., Aguirre, C.C., Tsoa, R.W., Kern, R.M., Grody, W.W., Cederbaum, S.D., and Iyer, R.K. (2003). Widespread expression of arginase I in mouse tissues: biochemical and physiological implications. J. Histochem. Cytochem. *51*, 1151–1160. https://doi.org/10.1177/002215540305100905.
51. Franklin, R.A. (2021). Fibroblasts and macrophages: collaborators in tissue homeostasis. Immunol. Rev. *302*, 86–103. https://doi.org/10.1111/imr.12989.
52. Öhlund, D., Handly-Santana, A., Biffi, G., Elyada, E., Almeida, A.S., Ponz-Sarvise, M., Corbo, V., Oni, T.E., Hearn, S.A., Lee, E.J., et al. (2017). Distinct populations of inflammatory fibroblasts and myofibroblasts in pancreatic cancer. J. Exp. Med. *214*, 579–596. https://doi.org/10.1084/jem.20162024.
53. Elyada, E., Bolisetty, M., Laise, P., Flynn, W.F., Courtois, E.T., Burkhart, R.A., Teinor, J.A., Belleau, P., Biffi, G., Lucito, M.S., et al. (2019). Cross-species single-cell analysis of pancreatic ductal adenocarcinoma reveals antigen-presenting cancer-associated fibroblasts. Cancer Discov. *9*, 1102–1123. https://doi.org/10.1158/2159-8290.CD-19-0094.
54. Dominguez, C.X., Müller, S., Keerthivasan, S., Koeppen, H., Hung, J., Gierke, S., Breart, B., Foreman, O., Bainbridge, T.W., Castiglioni, A., et al. (2020). Single-cell RNA sequencing reveals stromal evolution into LRRC15+ myofibroblasts as a determinant of patient response to cancer immunotherapy. Cancer Discov. *10*, 232–253. https://doi.org/10.1158/2159-8290.CD-19-0644.
55. Tsukui, T., Sun, K.H., Wetter, J.B., Wilson-Kanamori, J.R., Hazelwood, L.A., Henderson, N.C., Adams, T.S., Schupp, J.C., Poli, S.D., Rosas, I.O., et al. (2020). Collagen-producing lung cell atlas identifies multiple subsets with distinct localization and relevance to fibrosis. Nat. Commun. *11*, 1920. https://doi.org/10.1038/s41467-020-15647-5.
56. Buechler, M.B., Pradhan, R.N., Krishnamurty, A.T., Cox, C., Calviello, A.K., Wang, A.W., Yang, Y.A., Tam, L., Caothien, R., Roose-Girma, M., et al. (2021). Cross-tissue organization of the fibroblast lineage. Nature *593*, 575–579. https://doi.org/10.1038/s41586-021-03549-5.
57. Vu, R., Jin, S., Sun, P., Haensel, D., Nguyen, Q.H., Dragan, M., Kessenbrock, K., Nie, Q., and Dai, X. (2022). Wound healing in aged skin exhibits systems-level alterations in cellular composition and cell-cell communication. Cell Rep. *40*, 111155. https://doi.org/10.1016/j.celrep.2022.111155.
58. Hamilton, T.G., Klinghoffer, R.A., Corrin, P.D., and Soriano, P. (2003). Evolutionary divergence of platelet-derived growth factor alpha receptor signaling mechanisms. Mol. Cell. Biol. *23*, 4013–4025. https://doi.org/10.1128/MCB.23.11.4013-4025.2003.
59. Lee, D.D., and Seung, H.S. (1999). Learning the parts of objects by non-negative matrix factorization. Nature *401*, 788–791. https://doi.org/10.1038/44565.
60. Stein-O'Brien, G.L., Arora, R., Culhane, A.C., Favorov, A.V., Garmire, L.X., Greene, C.S., Goff, L.A., Li, Y., Ngom, A., Ochs, M.F., et al. (2018). Enter the matrix: factorization uncovers knowledge from omics. Trends Genet. *34*, 790–805. https://doi.org/10.1016/j.tig.2018.07.003.
61. Kotliar, D., Veres, A., Nagy, M.A., Tabrizi, S., Hodis, E., Melton, D.A., and Sabeti, P.C. (2019). Identifying gene expression programs of cell-type identity and cellular activity with single-cell RNA-Seq. eLife *8*, e43803. https://doi.org/10.7554/eLife.43803.

62. Pelka, K., Hofree, M., Chen, J.H., Sarkizova, S., Pirl, J.D., Jorgji, V., Bejnood, A., Dionne, D., Ge, W.H., Xu, K.H., et al. (2021). Spatially organized multicellular immune hubs in human colorectal cancer. Cell *184*, 4734–4752.e20. https://doi.org/10.1016/j.cell.2021.08.003.

63. DeBruine, Z.J., Melcher, K., and Triche, T.J., Jr. (2021). Fast and robust non-negative matrix factorization for single-cell experiments. https://doi.org/10.1101/2021.09.01.458620.

64. Pascual-Montano, A., Carazo, J.M., Kochi, K., Lehmann, D., and Pascual-Marqui, R.D. (2006). Nonsmooth nonnegative matrix factorization (nsNMF). IEEE Trans. Pattern Anal. Mach. Intell. *28*, 403–415. https://doi.org/10.1109/TPAMI.2006.60.

65. Elosua-Bayes, M., Nieto, P., Mereu, E., Gut, I., and Heyn, H. (2021). SPOTlight: seeded NMF regression to deconvolute spatial transcriptomics spots with single-cell transcriptomes. Nucleic Acids Res. *49*, e50. https://doi.org/10.1093/nar/gkab043.

66. Brunet, J.P., Tamayo, P., Golub, T.R., and Mesirov, J.P. (2004). Metagenes and molecular pattern discovery using matrix factorization. Proc. Natl. Acad. Sci. USA *101*, 4164–4169. https://doi.org/10.1073/pnas.0308531101.

67. Hongu, T., Pein, M., Insua-Rodríguez, J., Gutjahr, E., Mattavelli, G., Meier, J., Decker, K., Descot, A., Bozza, M., Harbottle, R., et al. (2022). Perivascular tenascin C triggers sequential activation of macrophages and endothelial cells to generate a pro-metastatic vascular niche in the lungs. Nat. Cancer *3*, 486–504. https://doi.org/10.1038/s43018-022-00353-6.

68. Gillan, L., Matei, D., Fishman, D.A., Gerbin, C.S., Karlan, B.Y., and Chang, D.D. (2002). Periostin secreted by epithelial ovarian carcinoma is a ligand for αVβ3 and αVβ5 integrins and promotes cell motility. Cancer Res. *62*, 5358–5364.

69. Schneider, W.M., Chevillotte, M.D., and Rice, C.M. (2014). Interferon-stimulated genes: A complex web of host defenses. Annu. Rev. Immunol. *32*, 513–545. https://doi.org/10.1146/annurev-immunol-032713-120231.

70. Davidson, S., Efremova, M., Riedel, A., Mahata, B., Pramanik, J., Huuhtanen, J., Kar, G., Vento-Tormo, R., Hagai, T., Chen, X., et al. (2020). Single-cell RNA sequencing reveals a dynamic stromal niche that supports tumor growth. Cell Rep. *31*, 107628. https://doi.org/10.1016/j.celrep.2020.107628.

71. Walz, A., Burgener, R., Car, B., Baggiolini, M., Kunkel, S.L., and Strieter, R.M. (1991). Structure and neutrophil-activating properties of a novel inflammatory peptide (ENA-78) with homology to interleukin 8. J. Exp. Med. *174*, 1355–1362. https://doi.org/10.1084/jem.174.6.1355.

72. Doni, A., Stravalaci, M., Inforzato, A., Magrini, E., Mantovani, A., Garlanda, C., and Bottazzi, B. (2019). The long pentraxin PTX3 as a link between innate immunity, tissue remodeling, and cancer. Front. Immunol. *10*, 712. https://doi.org/10.3389/fimmu.2019.00712.

73. Richards, C.D., Izakelian, L., Dubey, A., Zhang, G., Wong, S., Kwofie, K., Qureshi, A., and Botelho, F. (2016). Regulation of IL-33 by oncostatin M in mouse lung epithelial cells. Mediators Inflamm. *2016*, 9858374. https://doi.org/10.1155/2016/9858374.

74. Junk, D.J., Bryson, B.L., Smigiel, J.M., Parameswaran, N., Bartel, C.A., and Jackson, M.W. (2017). Oncostatin M promotes cancer cell plasticity through cooperative STAT3-SMAD3 signaling. Oncogene *36*, 4001–4013. https://doi.org/10.1038/onc.2017.33.

75. Yin, W., Li, Y., Song, Y., Zhang, J., Wu, C., Chen, Y., Miao, Y., Lin, C., Lin, Y., Yan, D., et al. (2021). CCRL2 promotes antitumor T-cell immunity via amplifying TLR4-mediated immunostimulatory macrophage activation. Proc. Natl. Acad. Sci. USA *118*, e2024171118. https://doi.org/10.1073/pnas.2024171118.

76. Liu, X., Zhang, Y., Yu, Y., Yang, X., and Cao, X. (2008). SOCS3 promotes TLR4 response in macrophages by feedback inhibiting TGF-β1/Smad3 signaling. Mol. Immunol. *45*, 1405–1413. https://doi.org/10.1016/j.molimm.2007.08.018.

77. Binnewies, M., Pollack, J.L., Rudolph, J., Dash, S., Abushawish, M., Lee, T., Jahchan, N.S., Canaday, P., Lu, E., Norng, M., et al. (2021). Targeting TREM2 on tumor-associated macrophages enhances immunotherapy. Cell Rep. *37*, 109844. https://doi.org/10.1016/j.celrep.2021.109844.

78. Katzenelenbogen, Y., Sheban, F., Yalin, A., Yofe, I., Svetlichnyy, D., Jaitin, D.A., Bornstein, C., Moshe, A., Keren-Shaul, H., Cohen, M., et al. (2020). Coupled scRNA-seq and intracellular protein activity reveal an immunosuppressive role of TREM2 in cancer. Cell *182*, 872–885.e19. https://doi.org/10.1016/j.cell.2020.06.032.

79. Molgora, M., Esaulova, E., Vermi, W., Hou, J., Chen, Y., Luo, J., Brioschi, S., Bugatti, M., Omodei, A.S., Ricci, B., et al. (2020). TREM2 modulation remodels the tumor myeloid landscape enhancing anti-PD-1 immunotherapy. Cell *182*, 886–900.e17. https://doi.org/10.1016/j.cell.2020.07.013.

80. Zhou, W., Ke, S.Q., Huang, Z., Flavahan, W., Fang, X., Paul, J., Wu, L., Sloan, A.E., McLendon, R.E., Li, X., et al. (2015). Periostin secreted by glioblastoma stem cells recruits M2 tumour-associated macrophages and promotes malignant growth. Nat. Cell Biol. *17*, 170–182. https://doi.org/10.1038/ncb3090.

81. Kormann, R., Kavvadas, P., Placier, S., Vandermeersch, S., Dorison, A., Dussaule, J.C., Chadjichristos, C.E., Prakoura, N., and Chatziantoniou, C. (2020). Periostin promotes cell proliferation and macrophage polarization to drive repair after AKI. J. Am. Soc. Nephrol. *31*, 85–100. https://doi.org/10.1681/ASN.2019020113.

82. González-González, L., and Alonso, J. (2018). Periostin: A matricellular protein with multiple functions in cancer development and progression. Front. Oncol. *8*, 225. https://doi.org/10.3389/fonc.2018.00225.

83. Combes, A.J., Samad, B., Tsui, J., Chew, N.W., Yan, P., Reeder, G.C., Kushnoor, D., Shen, A., Davidson, B., Barczak, A.J., et al. (2022). Discovering dominant tumor immune archetypes in a pan-cancer census. Cell *185*, 184–203.e19. https://doi.org/10.1016/j.cell.2021.12.004.

84. Harnik, Y., Buchauer, L., Ben-Moshe, S., Averbukh, I., Levin, Y., Savidor, A., Eilam, R., Moor, A.E., and Itzkovitz, S. (2021). Spatial discordances between mRNAs and proteins in the intestinal epithelium. Nat. Metab. *3*, 1680–1693. https://doi.org/10.1038/s42255-021-00504-6.

85. Henderson, N.C., Rieder, F., and Wynn, T.A. (2020). Fibrosis: from mechanisms to medicines. Nature *587*, 555–566. https://doi.org/10.1038/s41586-020-2938-9.

86. Eming, S.A., Murray, P.J., and Pearce, E.J. (2021). Metabolic orchestration of the wound healing response. Cell Metab. *33*, 1726–1743. https://doi.org/10.1016/j.cmet.2021.07.017.

87. Wynn, T.A., and Vannella, K.M. (2016). Macrophages in tissue repair, regeneration, and fibrosis. Immunity *44*, 450–462. https://doi.org/10.1016/j.immuni.2016.02.015.

88. Adler, M., Mayo, A., Zhou, X., Franklin, R.A., Meizlish, M.L., Medzhitov, R., Kallenberger, S.M., and Alon, U. (2020). Principles of cell circuits for tissue repair and fibrosis. iScience *23*, 100841. https://doi.org/10.1016/j.isci.2020.100841.

89. Hu, K.H., Eichorst, J.P., McGinnis, C.S., Patterson, D.M., Chow, E.D., Kersten, K., Jameson, S.C., Gartner, Z.J., Rao, A.A., and Krummel, M.F. (2020). ZipSeq: barcoding for real-time mapping of single cell transcriptomes. Nat. Methods *17*, 833–843. https://doi.org/10.1038/s41592-020-0880-2.

90. Lee, Y., Bogdanoff, D., Wang, Y., Hartoularos, G.C., Woo, J.M., Mowery, C.T., Nisonoff, H.M., Lee, D.S., Sun, Y., Lee, J., et al. (2021). Xyzeq: spatially resolved single-cell RNA sequencing reveals expression heterogeneity in the tumor microenvironment. Sci. Adv. *7*, eabg4755. https://doi.org/10.1126/sciadv.abg4755.

91. Rodriques, S.G., Stickels, R.R., Goeva, A., Martin, C.A., Murray, E., Vanderburg, C.R., Welch, J., Chen, L.M., Chen, F., and Macosko, E.Z. (2019). Slide-seq: A scalable technology for measuring genome-wide expression at high spatial resolution. Science *363*, 1463–1467. https://doi.org/10.1126/science.aaw1219.

92. Stoltzfus, C.R., Sivakumar, R., Kunz, L., Olin Pope, B.E., Menietti, E., Speziale, D., Adelfio, R., Bacac, M., Colombetti, S., Perro, M., et al. (2021). Multi-parameter quantitative imaging of tumor microenvironments reveals perivascular immune niches associated with anti-tumor

immunity. Front. Immunol. *12*, 726492. https://doi.org/10.3389/fimmu.2021.726492.

93. Asrir, A., Tardiveau, C., Coudert, J., Laffont, R., Blanchard, L., Bellard, E., Veerman, K., Bettini, S., Lafouresse, F., Vina, E., et al. (2022). Tumor-associated high endothelial venules mediate lymphocyte entry into tumors and predict response to PD-1 plus CTLA-4 combination immunotherapy. Cancer Cell *40*, 318–334.e9. https://doi.org/10.1016/j.ccell.2022.01.002.

94. Sanchez-Paulete, A.R., Cueto, F.J., Martinez-Lopez, M., Labiano, S., Morales-Kastresana, A., Rodriguez-Ruiz, M.E., et al. (2016). Cancer immunotherapy with immunomodulatory anti-CD137 and anti-PD-1 monoclonal antibodies requires BATF3-dependent dendritic cells. Cancer Discov. *6*, 71–79. https://doi.org/10.1158/2159-8290.CD-15-0510.

95. Kolter, J., Feuerstein, R., Zeis, P., Hagemeyer, N., Paterson, N., d'Errico, P., Baasch, S., Amann, L., Masuda, T., Lösslein, A., et al. (2019). A subset of skin macrophages contributes to the surveillance and regeneration of local nerves. Immunity *50*, 1482–1497.e7. https://doi.org/10.1016/j.immuni.2019.05.009.

96. Lorts, A., Schwanekamp, J.A., Baudino, T.A., McNally, E.M., and Molkentin, J.D. (2012). Deletion of periostin reduces muscular dystrophy and fibrosis in mice by modulating the transforming growth factor-β pathway. Proc. Natl. Acad. Sci. USA *109*, 10978–10983. https://doi.org/10.1073/pnas.1204708109.

97. Allard, D.E., Wang, Y., Li, J.J., Conley, B., Xu, E.W., Sailer, D., Kimpston, C., Notini, R., Smith, C.J., Koseoglu, E., et al. (2018). Schwann cell-derived periostin promotes autoimmune peripheral polyneuropathy via macrophage recruitment. J. Clin. Invest. *128*, 4727–4741. https://doi.org/10.1172/JCI99308.

98. Finck, R., Simonds, E.F., Jager, A., Krishnaswamy, S., Sachs, K., Fantl, W., Pe'er, D., Nolan, G.P., and Bendall, S.C. (2013). Normalization of mass cytometry data with bead standards. Cytometry A *83*, 483–494. https://doi.org/10.1002/cyto.a.22271.

99. Levine, J.H., Simonds, E.F., Bendall, S.C., Davis, K.L., Amir, E.A.D., Tadmor, M.D., Litvin, O., Fienberg, H.G., Jager, A., Zunder, E.R., et al. (2015). Data-driven phenotypic dissection of AML reveals progenitor-like cells that correlate with prognosis. Cell *162*, 184–197. https://doi.org/10.1016/j.cell.2015.05.047.

100. Stuart, T., Butler, A., Hoffman, P., Hafemeister, C., Papalexi, E., Mauck, W.M., Hao, Y., Stoeckius, M., Smibert, P., and Satija, R. (2019). Comprehensive Integration of Single-Cell Data. Cell *177*, 1888–1902.e21. https://doi.org/10.1016/j.cell.2019.05.031.

101. Gaujoux, R., and Seoighe, C. (2010). A flexible R package for nonnegative matrix factorization. BMC Bioinformatics *11*, 367. https://doi.org/10.1186/1471-2105-11-367.

102. Chen, W.S., Zivanovic, N., van Dijk, D., Wolf, G., Bodenmiller, B., and Krishnaswamy, S. (2020). Uncovering axes of variation among single-cell cancer specimens. Nat. Methods *17*, 302–310. https://doi.org/10.1038/s41592-019-0689-z.

103. Zunder, E.R., Finck, R., Behbehani, G.K., Amir, E.A.D., Krishnaswamy, S., Gonzalez, V.D., Lorang, C.G., Bjornson, Z., Spitzer, M.H., Bodenmiller, B., et al. (2015). Palladium-based mass tag cell barcoding with a doublet-filtering scheme and single-cell deconvolution algorithm. Nat. Protoc. *10*, 316–333. https://doi.org/10.1038/nprot.2015.020.

104. Spitzer, M.H., Carmi, Y., Reticker-Flynn, N.E., Kwek, S.S., Madhireddy, D., Martins, M.M., Gherardini, P.F., Prestwood, T.R., Chabon, J., Bendall, S.C., et al. (2017). Systemic immunity is required for effective cancer immunotherapy. Cell *168*, 487–502.e15. https://doi.org/10.1016/j.cell.2016.12.022.

105. Moon, K.R., van Dijk, D., Wang, Z., Gigante, S., Burkhardt, D.B., Chen, W.S., Yim, K., Elzen, A.V.D., Hirn, M.J., Coifman, R.R., et al. (2019). Visualizing structure and transitions in high-dimensional biological data. Nat. Biotechnol. *37*, 1482–1492. https://doi.org/10.1038/s41587-019-0336-3.

106. Qiu, X., Mao, Q., Tang, Y., Wang, L., Chawla, R., Pliner, H.A., and Trapnell, C. (2017). Reversed graph embedding resolves complex single-cell trajectories. Nat. Methods *14*, 979–982. https://doi.org/10.1038/nmeth.4402.

107. Cao, J., Spielmann, M., Qiu, X., Huang, X., Ibrahim, D.M., Hill, A.J., Zhang, F., Mundlos, S., Christiansen, L., Steemers, F.J., et al. (2019). The single-cell transcriptional landscape of mammalian organogenesis. Nature *566*, 496–502. https://doi.org/10.1038/s41586-019-0969-x.

STAR★METHODS

KEY RESOURCES TABLE

REAGENT or RESOURCE	SOURCE	IDENTIFIER
Antibodies		
anti-mouse CD16/32 (clone 2.4G2)	Tonbo Biosciences	70-0161-U500
anti-mouse CD45 Alexa Fluor 647 (clone 30-F11)	Biolegend	103124
anti-mouse GPNMB eFluor™ 660 (clone CTSREVL)	eBioscience	50-5708-80
anti-h/mPeriostin (clone 345613)	R&D Systems	MAB3548
anti-alpha smooth muscle actin antibody (polyclonal)	Abcam	AB5694
anti-mouse P-selectin (polyclonal)	R&D Systems	AF737
anti-CD31 AlexaFluor647 (clone 390)	BioLegend	102416
anti-CD11b AlexaFluor594 (clone M1/70)	BioLegend	101254
anti-CD206-AlexaFluor647 (clone C068C2)	BioLegend	141712
anti-I-A/I-E AlexaFluor594 (clone M5/114.15.2)	BioLegend	107650
anti-I-A/I-E AlexaFluor488 (clone M5/114.15.2)	BioLegend	107616
goat anti-rat IgG (H+L) AlexaFluor488	Thermo Fisher Scientific	A11006
donkey anti-goat IgG (H+L) AlexaFluor488	Thermo Fisher Scientific	A11055
F(ab')2-Goat anti-Rabbit IgG (H+L) Cross-Adsorbed Secondary Antibody, Alexa Fluor™ Plus 555	Thermo Fisher Scientific	A48283
Alexa Fluor® 488 AffiniPure Fab Fragment Goat Anti-Rat IgG (H+L)	Jackson ImmunoResearch	112-547-003
Alexa Fluor® 647 AffiniPure Fab Fragment Goat Anti-Rat IgG (H+L)	Jackson ImmunoResearch	112-607-003
anti-mouse B220 (clone RA3-6B2)	Biolegend	103202
anti-mouse CCR7 (clone 4B12)	Biolegend	120101
anti-mouse CD103 (clone 2e7)	Biolegend	121402
anti-mouse CD11b (clone M1/70)	Biolegend	101202
anti-mouse CD11c (clone N418)	Biolegend	117302
anti-mouse CD16/32 (clone 2.4G2)	BD	553142
anti-mouse CD19 (clone 6D5)	Biolegend	115501
anti-mouse CD206 (clone C068C2)	Biolegend	141702
anti-mouse CD207 (clone 4C7)	Biolegend	144202
anti-mouse CD24 (M1/69)	Biolegend	101802
anti-mouse CD3e (clone 17A2)	Biolegend	100202
anti-mouse CD38 (clone 90)	Biolegend	102702
anti-mouse CD4 (clone RM4-5)	Biolegend	100506
anti-mouse CD44 (clone IM7)	Biolegend	103002
anti-mouse CD45 (clone 30-F11)	Biolegend	103102
anti-mouse CD49b (clone HMa2)	Biolegend	103513
anti-mouse CD62L (clone MAB5671)	R&D	MAB5761
anti-mouse CD64 (clone (X54-5/7.1)	Biolegend	139302
anti-mouse CD69 (polyclonal)	R&D	AF2386
anti-mouse CD8a (clone 53-6.7)	Biolegend	100702
anti-mouse CD86 (clone GL-1)	Biolegend	105002
anti-mouse CD90 (clone G7)	Biolegend	105202

(*Continued on next page*)

Continued

REAGENT or RESOURCE	SOURCE	IDENTIFIER
anti-mouse c-Kit (clone 2B8)	Biolegend	105802
anti-mouse CTLA-4 (clone UC10-4B9)	Biolegend	106302
anti-mouse F4/80 (clone BM8)	Biolegend	123102
anti-mouse FceR1a (clone MAR-1)	Biolegend	134302
anti-mouse Foxp3 (clone NRRF-30)	eBiosciences	14-4771-80
anti-mouse GATA3 (clone 16E10A23)	Biolegend	653802
anti-mouse Ki67 (clone SolA15)	eBiosciences	14-5698-82
anti-mouse Ly6C (clone HK1.4)	Biolegend	128002
anti-mouse Ly6G (clone 1A8)	Biolegend	127602
anti-mouse MHC-II (clone M5/114.15.2)	Biolegend	107602
anti-mouse PD-1 (clone 29F.1A12)	Biolegend	135202
anti-mouse PD-L1 (clone 10F.9G2)	Biolegend	124302
anti-mouse PDCA1 (clone 927)	Biolegend	127002
anti-mouse RORgt (clone B2D)	eBiosciences	14-6981-82
anti-mouse Siglec F (clone E50-2440)	BD Biosciences	552125
anti-mouse SIRPa (clone P84)	Biolegend	144002
anti-mouse T-bet (clone 4B10)	Biolegend	644802
anti-mouse TCRgd (clone GL3)	Biolegend	118101
anti-mouse Ter119 (clone Ter119)	Biolegend	116202
anti-mouse TIM-3 (clone B8.2C12)	Biolegend	134002
anti-human CD45 APC/e780 (clone HI30)	Thermo Fisher	47-0459-42
anti-human CD3e PerCP/e710 (clone OKT3)	Thermo Fisher	46-0037-42
anti-human HLA-DR BUV395 (clone G46-6)	BD Biosciences	564040
Biological samples		
Fetal Bovine Serum, Benchmark	GeminiBio	100-106
Chemicals, peptides, and recombinant proteins		
Methanol	Fisher Scientific	A412-4
recombinant human Tenascin	Merck Millipore	CC-065
recombinant mouse Periostin	R&D Systems	2955-F2-050
recombinant mouse Oncostatin M	BioLegend	762802
Albumin, Bovine (BSA), nuclease free	VWR	332
Albumin, Bovine (BSA)	Sigma	A7906
EDTA	Teknova	E0306
Maxpar PBS	Fluidigm	201058
Maxpar Cell Staining Buffer	Fluidigm	201068
Maxpar Water	Fluidigm	201069
EQ Four Element Calibration Beads	Fluidigm	201078
Saponin	Sigma	S-7900
Cisplatin	Enzo Life Sciences	ALX-400-040
NaN3	Sigma	S-8032
Cell-ID 20-Plex Pd Barcoding Kit	Fluidigm	201060
Cell-ID 125 μm Iridium Intercalator	Fluidigm	201192A
16% paraformaldehyde	Electron Microscopy Sciences	15710
DNase I	Millipore Sigma	10104159001
Collagenase IX	Millipore Sigma	C7657
Hyaluronidase	Worthington Biochemical Corp	LS005477
buprenorphine hydrochloride	Hospira	0409-2012-32

(*Continued on next page*)

Continued

REAGENT or RESOURCE	SOURCE	IDENTIFIER
bupivicaine	AuroMedica Pharma LLC	55150-167-10
OCT	Sakura	4583
Triton X-100	Sigma	T8787
Mouse serum	Jackson ImmunoResearch	015-000-120
Normal rat serum	Stem Cell Technologies	13551
Goat serum	Sigma	G9023
Histodenz	Sigma	D-2158
N-methylacetamide	Sigma	M26305-100G
1-Thioglycerol	Sigma	M1753-100ML
5X iScript RT Supermix	Bio-Rad	L001404B
SsoFast EvaGreen Supermix	Bio-Rad	L000915B
Critical commercial assays		
Chromium Next GEM Single Cell 3' GEM, Library & Gel Bead Kit v3.1, 16 rxns	10x Genomics	PN1000121
Chromium Next GEM Chip G Single Cell Kit, 48 rxns	10x Genomics	PN-1000120
Chromium Next GEM Single Cell 5' Library & Gel Bead Kit v1.1, 16 rxns	10x Genomics	PN-1000165
10X Chromium Controller	10x Genomics	N/A
Deposited data		
Mouse spatiotemporal scRNAseq wound data set	This paper	GEO: GSE204777
Human tumor scRNAseq data set	This paper	https://doi.org/10.17632/nnmb6m5p5j.1
Mouse melanoma fibroblast data set	Davidson et al.[70] (PMID: 32433953)	ArrayExpress: E-MTAB-7427
Mouse pan-tissue fibroblast scRNAseq atlas	Buechler et al.[22] (PMID: 33981032)	ArrayExpress:E-MTAB-10315
Mouse pancreatic cancer fibroblast sc RNAseq data set	Dominguez et al.[54] (PMID: 31699795)	ArrayExpress: E-MTAB-8483
Mouse wound scRNAseq data set	Guerrero-Juarez et al.[26] (PMID: 31699795)	GEO: GSE113854
Supplementary Mendeley Figures & Tables	Mendeley Data	Mendeley data: https://doi.org/10.17632/kmmw43j2z6.2
Experimental models: Cell lines		
B16-F10 (mouse melanoma cell line)	ATCC	CRL-6475
MC38 (mouse colorectal tumor cell line)	Kerafast	ENH204-FP
Experimental models: Organisms/strains		
Mouse: wild-type C57BL/6	The Jackson Laboratory	Stock# 000664
Mouse: Arg1-tdTomato-CreERT2 x R26R-EYFP	H.-E. Liang and R. Locksley (UCSF)[49]	https://www.sciencedirect.com/science/article/pii/S1074761319301992
Mouse: *Pdgfra*-H2B-EGFP	A. Molofsky (UCSF)[58]	Stock# 007669,
Oligonucleotides		
See Table S2 for qPCR primers	IDT	N/A
Software and algorithms		
Original code for analysis and figure generation	This Paper	https://github.com/ken7hu/WH_SpaceTime
Normalizer	Finck et al.[98]; https://onlinelibrary.wiley.com/doi/10.1002/cyto.a.22271	https://rdrr.io/bioc/CATALYST/man/normCytof.html

(*Continued on next page*)

Continued

REAGENT or RESOURCE	SOURCE	IDENTIFIER
Rphenograph	Levine et al.[99]; https://www.sciencedirect.com/science/article/pii/S0092867415006376	https://github.com/JinmiaoChenLab/Rphenograph
R environment	R Development Core Team	https://cran.r-project.org/bin/windows/base/
Premessa	Parker ICI	https://github.com/ParkerICI/premessa
Flow Jo v10.8.1	Tree Star	https://www.flowjo.com/
Imaris 9.2.1	Bitplane	https://imaris.oxinst.com/products/imaris-for-cell-biologists?gad=1&gclid=Cj0KCQjw3a2iBhCFARIsAD4jQB2RkztA4vyhmDUQ3_eo2WwjysDt-NhFrH-evt8PxW5s5oKpw_WYJhcaAuhZEALw_wcB
MATLAB	The MathWorks, Inc.	https://www.mathworks.com/products/matlab.html
LASX	Leica Microsystems	https://www.leica-microsystems.com/products/microscope-software/p/leica-las-x-ls/
CellChat (R package)	Jin et al.[10]; https://www.nature.com/articles/s41467-021-21246-9	https://github.com/sqjin/CellChat
Seurat v3 (R package)	Stuart et al.[100] [Seurat V3]	https://satijalab.org/seurat/
NMF (R package)	Gaujoux and Seoighe[101], http://www.biomedcentral.com/1471-2105/11/367.	https://cran.r-project.org/web/packages/NMF/index.html
Corrplot (R package)	https://cran.r-project.org/web/packages/corrplot/vignettes/corrplot-intro.html	https://cran.r-project.org/web/packages/corrplot/vignettes/corrplot-intro.html
Ggpubr (R package)	https://cran.r-project.org/web/packages/ggpubr/index.html	https://cran.r-project.org/web/packages/ggpubr/index.html
PhEMD	Chen et al.[102]; https://www.nature.com/articles/s41592-019-0689-z	https://www.bioconductor.org/packages/release/bioc/html/phemd.html
Monocle 3	Trapnell et al.[43]; https://doi.org/10.1038/nbt.2859	https://github.com/cole-trapnell-lab/monocle3
CellRanger v 4.0.0	10X Genomics	https://support.10xgenomics.com/single-cell-gene-expression/software/downloads/latest
Biorender	https://www.biorender.com	https://www.biorender.com/
Other		
lipid-modified oligonucleotides (LMO)	McGinnis et al.[37]; https://www.nature.com/articles/s41592-019-0433-8	N/A
MaxPAR antibody conjugation kit	Fluidigm	201146B
Dermal biopsy punch, 2 mm	Acuderm inc.	69038-02
Dermal biopsy punch, 4 mm	Integra	33-34
Dermal biopsy punch, 6 mm	Integra	33-36
Dermal biopsy punch, 8 mm	Integra	33-37
RNeasy Mini Kit	Qiagen	74104

RESOURCE AVAILABILITY

Lead contact

Further information and requests for resources and reagents should be directed to and will be fulfilled by the lead contact, Matthew F. Krummel (matthew.krummel@ucsf.edu).

Materials availability

This study did not generate new unique reagents.

Data and code availability

- Original and publicly available single-cell RNA-seq data have been deposited in GEO and Mendeley Data and are publicly available as of the date of publication. Accession numbers/DOIs are listed in the key resources table.
- All original code has been deposited at Github and is publicly available as of the date of publication. DOIs are listed in the key resources table.
- Any additional information required to reanalyze the data reported in this paper is available from the lead contact upon request.

EXPERIMENTAL MODEL AND STUDY PARTICIPANT DETAILS

Animals

All mice were housed in an American Association for the Accreditation of Laboratory Animal Care (AALAC)-accredited animal facility and maintained in specific pathogen-free conditions. All animal experiments were approved and performed in accordance with the Institutional Animal Care and Use Program protocol number AN184232. Wild-type female C57BL/6 mice between 6-12 weeks old were purchased from The Jackson Laboratory, *Arg1-tdTomato*^{CreERT2} x *R26R-EYFP* mice were a kind gift from Drs. Hong-Erh Liang and Richard Locksley (UCSF), *Pdgfra*-H2B-EGFP$^{+/wt}$ mice were a kind gift from Dr. Ari Molofsky (UCSF). All mice were housed at the University of California, San Francisco (UCSF) animal facility with typical light/dark cycles and standard chow. For tumor growth studies, MC38 colon cancer ($5x10^5$ cells / 50 μl) or B16-F10 melanoma cancer cells ($1x10^5$ cells / 50 ul) were transplanted into the subcutaneous region of the mouse flank. On day 14 after tumor challenge, when tumors reached a size/volume of approximately 0.5 cm^3, mice were sacrificed, tumors were excised and processed for downstream analysis.

Cell lines

B16-F10 and MC38 cells were purchased from ATCC and Kerafast, respectively, and cultured at 37°C in 5% CO_2 in DMEM supplemented with 10% FBS (Benchmark), 2 mM L-glutamine, 100 U/ml penicillin, and 100 μg/ml streptomycin.

Human tumor collection of the UCSF Immunoprofiler Initiative (IPI)

Tumor samples for the Immunoprofiler was transported from various cancer operating rooms (ORs). All patients consented by the UCSF IPI clinical coordinator group for tissue collection under a UCSF IRB approved protocol (UCSF IRB# 20-31740). Samples were obtained after surgical excision with biopsies taken by Pathology Assistants to confirm the presence of tumor cells. Patients were selected without regard to prior treatment. Freshly resected samples were placed in ice-cold PBS or Leibovitz's L-15 medium in a 50 mL conical tube and immediately transported to the laboratory where they were chopped in small pieces (2-3mm^2) and placed in a cryovial filled with 1mL of freezing media (10% DMSO, 90% FBS) and stored at -80 in a Polycarbonate container, blue high-density polyethylene closure, white high-density polyethylene vial holder overnight. The cryovials were then moved to a nitrogen tank for long-term storage.

Human tissue digestion and cell sorting for single cell RNA sequencing analysis

Tumor tissue contained in a cryovial was rapidly thawed in a 37C water bath and then the tissue was rinsed 3 times in complete media (RPMI with 10% FBS) before being thoroughly chopped with surgical scissors and transferred to GentleMACs C Tubes (Miltenyi Biotec) containing 20 uL/mL Liberase TL (5 mg/ml, Roche) and 50 U/ml DNAse I (Roche) in RPMI 1640 per 0.3 g tissue. GentleMACs C Tubes were then installed onto the GentleMACs Octo Dissociator (Miltenyi Biotec) and incubated for up to 45min according to the manufacturer's instructions. Samples were then quenched with 15 mL of sort buffer (PBS/2% FBS/2mM EDTA), filtered through 100 μm filters and spun down. Red blood cell lysis was performed with 175 mM ammonium chloride if needed. Cells were then incubated with Human FcX (BioLegend) to prevent non-specific antibody binding. Cells were then washed in DPBS and incubated with Zombie Aqua Fixable Viability Dye (Thermo). Following viability dye incubation, cells were washed with sort buffer and incubated with cell surface antibodies mix diluted (containing anti-human CD45, anti-human CD3e, and anti-human HLA-DR) in the BV stain buffer (BD Biosciences) following manufacturer instruction for 30 minutes on ice in the dark. Cells were then washed three times and resuspended in sort buffer (PBS/2% FBS/2mM EDTA) after filtering through a 100 μm filter prior to flow sorting. Each sample was then sorted for viable immune cell ($CD45^+$ viability dye^-) and viable non-immune cells ($CD45^-$ viability dye^-). Each sample was enriched for immune cells at a ratio of 80% immune and 20% non-immune cells. After sorting, cells were pelleted and resuspended at 10^3 cells/ul in 0.04%BSA/PBA and loaded onto the Chromium Controller (10X Genomics). Samples were processed for single-cell encapsulation and cDNA library generation using the Chromium Single Cell 5' v1.1 Reagent Kits (10X Genomics). The library was subsequently sequenced on an Illumina Novaseq (Illumina). All samples were sequenced at 25,000 reads per cell.

METHOD DETAILS

Full-thickness wounding

All mice used for wounding experiments were between 7-10 weeks old (second telogen hair follicle phase). Two to four days before wounding, back skin was shaved and residual hair was removed using NAIR (Walgreens). On the day of wounding, mice were anesthetized with 3% isofluorane and subcutaneously injected with 50 μl of 0.25% bupivacaine and 50 μl of 50 μg/ml buprenorphine for analgesia. The back skin was then sterilized using a Betadine Solution swab stick (for scRNAseq and imaging experiments) or ChloraPrep (BD Biosciences) (for Mass Cytometry experiments to avoid iodine contamination during sample acquisition). Four full-thickness wounds were generated with a 4 mm biopsy punch. Wound diameter was measured with calipers.

Tissue Processing

At time of analysis, mice were euthanized, back skin was dissected from mice, excess scapular and inguinal fat was removed, and wounds plus adjacent tissue was excised using an 8 mm biopsy punch. An 8 mm biopsy punch was used to collect unwounded back skin as a day 0 or unwounded control. Four to six 8 mm biopsy punches were pooled from unwounded back skin to collect sufficient cells for downstream analysis. On ice, tissue was finely minced with scissors and then placed in a 2 ml tube containing 1 ml of digestion medium (2 mg/ml collagenase XI, 0.5 mg/ml hyaluronidase, 0.1 mg/ml DNase in RPMI with 10% FBS, 2 mM L-glutamine, 100 U/ml penicillin, 100 μg/ml streptomycin, 50 μM beta-mercaptoethanol). The tube was placed horizontally in a bacterial shaker for 45 min at 37°C and 225 rpm. The sample was then filtered through a 100 μm filter and washed with 10 ml cold RPMI. The generated single cell suspension was then processed for further depending on analysis method.

Mass Cytometry

Antibody conjugate generation

All mass cytometry antibodies are listed in the key resources table. Primary conjugates of mass cytometry antibodies were prepared using the MaxPAR antibody conjugation kit (Fluidigm) according to the manufacturer's instructions. After labeling, antibodies were diluted in Candor PBS Antibody Stabilization solution (Candor Bioscience GmbH, Wangen, Germany) containing 0.02% NaN3 at 0.1-0.3 mg/ml. Antibody conjugates were stored at 4°C. Each antibody clone and lot was titrated to optimal staining concentrations.

Cell Preparation

After single cell generation, cells were resuspended at $1x10^6$ cells / ml PBS with 5 mM EDTA. An equal volume of PBS with 5 mM EDTA plus 50 μM Cisplatin (Enzo Life Sciences, Farmingdale, NY) was added and incubated for 60 s before quenching with an equal volume of PBS with 5 mM EDTA plus 0.5% BSA. Cells were centrifuged at 500 g for 5 min at 4°C. Washed cells were resuspended in PBS with 5 mM EDTA and fixed with 2.67% PFA for 10 min at RT. Fixation was quenched by adding 10x volume of PBS with 5 mM EDTA plus 0.5% BSA. Cells were centrifuged at 500 g for 5 min at 4°C and resuspended in PBS with 0.5% BSA and 10% DMSO before frozen and stored at -80°C until barcoding.

Mass-Tag Cellular Barcoding

After thawing stored samples at RT, up to $1x10^6$ cells from each mouse were barcoded with distinct combinations of stable Pd isotopes in PBS with 0.02% saponin as described before.[103] After incubation at RT for 15 min on a shaker at 90 rpm, cells were pelleted at 600 g for 5 min at 4°C and washed two more times with cell staining media (CSM: PBS with 0.5% BSA and 0.02% NaN3). After the last wash, all samples were pooled into a single 15 ml tube.

Mass Cytometry Staining and Acquisition

After barcoding and pooling of samples, all cells were pelleted at 600 g for 5 min at 4°C and resuspended in CSM containing a metal-labeled anti-CD16/32 antibody for 5 min at RT on shaker at 90 rpm to block Fc receptors. Extracellular cell markers were stained by adding a master mix of metal-labeled antibodies listed in the key resources table. After incubation for 30 min at RT on a shaker at 90 rpm, cells were washed with 5 ml of CSM. For cell permeabilization prior to intracellular stain, pelleted cells were resuspended in 1 ml of pre-chilled 99% MeOH (Sigma Aldrich) and incubated for 10 min at 4°C. Cells were washed twice in 5 ml of CSM prior to intracellular stain. For intracellular staining, pelleted cells were resuspended in the master mix of metal-labeled antibodies for intracellular targets and incubated for 30 min at RT on a shaker 90 rpm. Cells were washed with 5 ml of CSM and then resuspended in 2 ml PBS with 1.6% PFA and 0.55 μl 191/193Ir DNA Intercalator (Fluidigm). Cells were incubated overnight at 4°C. Cells were then washed once with 12 ml CSM, once with 12 ml PBS, and once with 12 ml of ddH_2O prior to dilution in H_2O at about $3x10^6$ cells/ml containing normalization beads (see below), filtered through a 70 μm cell strainer and then analyzed on a Helios mass cytometer (Fluidigm, San Francisco, CA). We analyzed $3x10^4$-$2x10^5$ cells per sample.

Mass Cytometry Bead Standard Data Normalization

Data normalization was performed as previously described.[104] All mass cytometry files were normalized together using the mass cytometry data normalization algorithm,[98] which uses the intensity values of a sliding window of the bead standards to correct for instrument fluctuations over time and between samples.

Data Analysis

After bead normalization and debarcoding using the Premessa package (https://github.com/ParkerICI/premessa), singlets were gated by Event Length and DNA content. Live cells were identified as Cisplatin-negative cells. Immune cells were identified as $CD45^+$ cells and downsampled to 3.000-10.000 cells per sample prior to export and concatenation in FlowJo (Treestar). After concatenation of all cells from each timepoint, cell clusters were identified using the Phenograph algorithm[99] using k=190 nearest neighbors. Mean intensity values

of each marker per cluster were exported from FlowJo and imported into Morpheus (https://software.broadinstitute.org/morpheus/) to generate heatmaps. The identity of each cluster was determined based on expression of stained markers.

Cell counts ber sample and CyTOF run can be found in Mendeley Table S1 at https://doi.org/10.17632/kmmw43j2z6.2.

Single cell RNA sequencing of skin wound-associated cells

For spatiotemporal scRNAseq analysis, skin wounds were processed as described above to generate single cell suspensions, except that after excising the skin wound and adjacent tissue with an 8 mm biopsy punch, the excised skin wounds were further partitioned by successively using a 2 mm, 4 mm, and 6 mm biopsy punch, resulting in three rings and one round center sample, all with different diameters (Figure 1A). Digestion of tissue proceeded as described above, except that no DNase I was used in the digestion media to avoid potential downstream cleaving of nucleotide barcodes. After washing and pelleting of cells at 500 g for 5 min at 4, samples were each resuspended in 100 μl of staining buffer (PBS plus 2% FBS and 2 mM EDTA) and 2 μl of purified anti-mouse CD16/32 (Fc Shield, clone 2.4G2, Tonbo Biosciences, 2 mg/ml) was added to the sample. Samples were incubated for 15′ on ice to block FC receptors. Following this incubation, anti-mouse CD45 Alexa Fluor 647 (clone 30-F11, Biolegend, 1:1000) was added and cells were incubated for an additional 20' on ice. Cells were washed using staining buffer, pelleted at 500 g for 5 min, and resuspended in staining buffer plus DAPI (1 μM). Cells were filtered on a 40 μm cell strainer right before being sorted on a BD FACSAria II cell sorter (BD Biosciences). $CD45^+$ and $CD45^-$ cells were collected separately in ice cold collection buffer (colorless RPMI supplemented with 10% FBS, 2 mM L-glutamine, 100 U/ml penicillin, 100 μg/ml streptomycin, 50 μM beta-mercaptoethanol). Across all 17 samples (= 4 timepoints multiplied by 4 areas plus one unwounded sample), 206 x 10^3 $CD45^+$ and 263.7 x 10^3 $CD45^-$ cells were collected. Cells of individual samples were pelleted at 500 g for 5 min at 4°C. Supernatant was removed and cells were resuspended in 160 μl of colorless RPMI. Samples were then barcoded using lipid modified oligonucleotides (LMO) as in McGinnis et al.[37] before pooling. The pool was then split over 5 lanes of a 10X 3' NEXTGEM chip before encapsulation with a targeted cell number of 12,000 per lane.

Following the MULTI-Seq library construction protocol, additive primer was spiked in during the cDNA amplification step as described in McGinnis et al.,[37] the supernatant was reserved following SPRI cleanup and separately amplified. Finally, libraries were pooled for sequencing using a 1:10 molar ratio of LMO: gene expression (GEX) libraries with approximately equal representation from each lane. Pooled samples were then sequenced using 1 lane of a S4 flowcell for a target of ~3B reads. GEX libraries had total read counts of (493M, 515M, 495M, 452M, 403M) for lanes (1,2,3,4,5) respectively, showing similar order of magnitude representation in read counts. The estimated sequencing saturation ranged from 58-64% (calculated via CellRanger), indicating sequencing depth did not vary appreciably between lanes. LMO libraries had total read counts of (37M, 39M, 38M, 36M, 32M) also showing stable representation from all 5 lanes.

Each individual well was demultiplexed using deMULTIplex package[37] to remove doublets and unlabeled cells. Confidently hashed cells were then carried forward for integration in Seurat v3.[100] From there, cells with percent mitochondrial reads >25 percent and number of genes <200 were filtered out. Following an initial high-level clustering, we removed several clusters composed mostly of high mitochondrial % cells or low nUMI and a immune/non-immune doublet cluster. An initial high-level clustering and dimensional reduction was used to define the $CD45^+$ and CD45- subsets. Once subsetted, each group was then further re-clustered to generate the 'final' $CD45^+$/- datasets.

Candidate identification of ligand-receptor interactions using CellChat

For CellChat analysis,[10] the M/M subset and fibroblast subsets were merged into a single Seurat object, then split into 5 Seurat objects based on the 'Day' metadata. Each Seurat object was then imported into a CellChat object using the 'RNA' assay. Signaling network likelihoods were calculated using CellChat's computeCommunProb function using the trimean method, using raw data, and with population size scaling. Stacked barchart was calculated using the rankNet function with genes ordered by day weighted average.

Embedding a low-dimensional representation of samples using PhEMD

For mass cytometry data, PhEMD was employed to generate a two- or three-dimensional embedding of all samples split by timepoint based on their immune cell profiles.[102] For scRNAseq data, a two-dimensional embedding of $CD45^+$ samples split by all space/timepoints based on their immune cell profiles was generated. Briefly, PhEMD first generates a reference map of cell subtypes, then uses Earth Mover's Distance (EMD) to compute pairwise dissimilarities between samples (incorporating sample-to-sample differences in cell fractions of each cell subtype as well as intrinsic dissimilarities between subtypes based on the cell subtype reference map), and finally applies a dimensionality reduction technique to the sample-to-sample distance matrix to generate a final embedding of samples. The Seurat implementation of 3D Uniform Manifold Approximation and Projection (UMAP) was used to map the cell-subtype space. Dissimilarity between each pair of cell subtypes was defined as the distance between the centroids (in UMAP space) of all cells assigned to the two respective subtypes. PHATE was applied to the EMD patient-to-patient distance matrix to generate the final 3D embedding of samples.[105]

For PhEMD application to CyTOF data, the fully concatenated clean datasets were converted into feature-cell sparse matrices that Seurat could import, analogous to a scRNA-Seq dataset. The data was then transformed using the arcsinh transform and processed as described above.

Pseudotime Analysis in scRNAseq data set

Monocle analysis

Raw counts from the individual cell-specific object were used to create a Monocle3[43,106,107] cell_data_set object, and the PCA and UMAP embeddings were imported directly from the Seurat object. Each cell-specific trajectory was inferred by reverse embedding the UMAP coordinates using the DDRTree method. The root cell states for the trajectory in the MHCII^{low} and MHCII^{hi} Mono_Mac objects were chosen based on which cell cluster was present on day 1 post-wounding. Relative pseudotime was obtained through a linear transformation relative to the cells with the lowest and highest pseudotimes ((1 - *min_pseudotime*) / *max_pseudotime*).

Space/Time Tileplot of pseudotime

Similar to the Space/Time Tileplot of cell frequencies described above, a tileplot for the MHCII^{low} and MHCII^{hi} Mono_Macs was created. The numbers in each tile represent the average pseudotime value of all cells found at that particular space/timepoint. 'D00' represents cells found in the unwounded skin and, therefore, is not split into different wound regions.

Ce3D Tissue Clearing and Whole Mount Imaging

Tissue staining and clearing

Wounds and surrounding tissue were excised from back skin using an 8 mm biopsy punch. Wound samples were cleared using the Ce3D clearing protocol[46] with minor modifications. First, wound samples were fixed in 4% PFA (16% PFA, Electron Microscopy Sciences, diluted in PBS) at 4°C overnight on a horizontal shaker at 100 rpm by sandwiching them between two layers of cell strainer mesh to prevent sample curling. Subsequent steps were all performed protected from light. One wound sample was then transferred into a 2 ml tube and washed three times 30–60 min in 1 ml of wash buffer (PBS, 0.3% Triton X-100, 0.5% 1-thioglycerol) on a horizontal shaker at RT at 100 rpm. The inside of the 2 ml tube lid was plugged with a polydimethylsiloxane (PDMS) cut out to prevent the sample from being stuck during all subsequent washing, blocking, staining, and clearing steps. After washing, the sample was immersed in filtered blocking solution (PBS, 0.3% Triton X-100), 1% BSA, 1% normal mouse serum, and 1% normal serum of host species of used staining antibodies) overnight at 37°C on a horizontal shaker at 100 rpm. The next day, the sample was stained in 1 ml blocking buffer supplemented with DAPI (1 ug/ml) for nuclear staining, anti-CD49f/ITGA6 AF488 (clone GoH3; 1:100, stock 200 μg/ml), anti-CD11b AF647 (clone M1/70; 1:100, stock 500 μg/ml), anti-CD11b AF594 (clone M1/70; 1:100, stock 500 μg/ml), and/or anti-CD206 AF647 (clone C068C2; 1:200, stock 500 μg/ml) antibodies. The sample was incubated for three days at 37°C on a horizontal shaker at 100 rpm. After the staining incubation, the sample was transferred into a new 2 ml tube and washed once using 1 ml wash buffer for 8-12 h at 37°C on a horizontal shaker at 100 rpm, and then three more times with 1 ml wash buffer for 8-12 h at RT on a horizontal shaker at 100 rpm. After washing, the sample was transferred into a new 2 ml tube for clearing by subsequently incubating the sample in 1 ml of 33%, 50%, 80%, or 100% Ce3D clearing solution (2.75 ml 40% N-methylacetamide, 4 g Histodenz, 5 μl Triton X-100, 25 μl 1-thioglycerol) diluted in wash buffer at RT on a horizontal shaker at 100 rpm. The 33%, 50%, and 80% Ce3D clearing steps were done for 1 h each and the 100% clearing step was done overnight. After clearing, the sample was mounted epidermal side facing down on a PDMS chamber that fit the sample in the middle. Ce3D clearing solution was used as the mounting medium.

'Thick' section clearing

For 'thick' section (250-300 μm) clearing and imaging for both wounds and tumor samples, we started with whole tissue (wound or tumor) and fixed with 4% PFA at 4C overnight. This was followed by a progressive 15% to 30% w/v sucrose gradient then embedding and freezing in OCT. Thick sections were then made using a cryostat and placed into PBS to wash OCT residue away. These sections were then carried through a generalized Ce3D workflow.[12] Blocking and wash buffers same as above. For the POSTN and αSMA staining in Figures 3 and S3, we used the following primary antibodies for 1 day at 37C followed by 1 day at RT in Ce3D blocking buffer supplemented with 1% Normal Goat Serum: anti-aSMA (1:200 Abcam stock at 0.2mg/mL) and anti-POSTN (1:200 R&D stock 500 μg/ml). Following a 1 day wash, we stained with the following secondaries for 2 days at RT: Goat anti-rabbit F(ab')2 AF555 (1:1000, Thermo stock 2 mg/mL) and Goat anti rabbit F(ab) AF647 (1:1000, Jackson Immuno stock 1.25 mg/mL) and DAPI at 2 ug/mL. Samples were then washed for another day before clearing and mounting as above.

For imaging of Selectin-P and CD31 vasculature in thick tumor sections in Figure 7, sections were blocked in Ce3D blocking buffer with 1% NDS and NRS, then stained with primary anti mouse P-selectin (1:200, R&D stock 0.2 mg/mL) and anti-CD31 (1:100) and. After washing, we applied to following stains: donkey anti-goat AF488 (1:1000, Thermo stock 2mg/mL), anti-CD31 (1:100, Biolegend 0.5 mg/mL) and anti-I-A/I-E AlexaFluor594 (1:200, Biolegend stock 0.5mg/mL) and DAPI at 2 ug/mL. Following staining, thick sections were cleared as above and mounted in additional clearing solution in cavity slides, then cover slipped.

'Thin' cryosection imaging

For thin (10 μm) sections, samples were embedded and frozen in OCT, then sectioned on the cryostat and transferred to slides. Samples were then fixed 2 hr 4C in 4% PFA before permeabilization for 15 min in 0.2% Triton X-100. Samples were then blocked using (PBS, 0.1% Triton X-100), 1% BSA, and 1% normal serum of host species of used staining antibodies) and stained in the same buffer. All staining steps were performed at 4C overnight. For thin sections of wounds in Figure S4, we first stained for POSTN using rat-derived anti-human/mouse periostin antibody (clone 345624, R&D Systems, 1:200, stock 500 μg/ml) and secondary AF488 goat anti-rat F(ab) (1:1000, stock 2 mg/mL). Following washing and blocking with Normal Rat Serum, we stained with anti-mouse GPNMB eFluor660 (clone CTSREVL, ThermoFisher, 1:200, 200 μg/ml) as well as 1 ug/mL DAPI. For thin tumor sections in Figure 7, we first stained for POSTN using rat-derived anti-human/mouse periostin antibody (clone 345624, R&D Systems, 1:200, stock 500 μg/ml) and secondary AF488 goat anti-rat F(ab) (1:1000, stock 2 mg/mL) as above Following washing and blocking with Normal

Rat Serum, we stained with anti-mouse CD11b AF594 (Biolegend clone M1/70; 1:100, stock 500 μg/ml) as well as 1 ug/mL DAPI. Slides were washed and coverslipped using VectaShield.

Image acquisition and analysis

All samples were imaged using a Leica SP8 laser scanning confocal microscope with a white light laser and 405 nm diode. For whole cleared wounds, a 16X 0.6NA (HC Fluotar L 16x/0.6 IMM CORR DLS, Leica) objective was used during acquisition. 'Thick' (250-300 μm) and 'thin' (10 μm) cryosections were imaged using a 20X 0.75NA (HC PL APO 20x/0.75 IMM CORR CS2, Leica) objective. After acquisition, individual tiled images were stitched together using the LAS X software (Leica) and then analyzed using the Imaris software suite (Bitplane).

Imaris processing

For large volume images, spots were created using the Imaris Spots function and inputting the DAPI nuclear stain signal. Parameters for Spots generation are listed in Mendeley Table S2 at https://doi.org/10.17632/kmmw43j2z6.2. This first step is done to locate and identify individual cells within the imaged sample. Spherical spots here are created based on signal above a user-defined threshold value in the DAPI channel and based on the size of the DAPI object. Next, Surfaces for channels CD11b, Arg1-tdTomato, and CD206 were created based on the parameters listed in Mendeley Table S2 at https://doi.org/10.17632/kmmw43j2z6.2 using the Imaris Surfaces function. Surface marker-positive cells were identified by their vicinity to a previously identified DAPI spot. Depending on surface marker (see Mendeley Table S2 at https://doi.org/10.17632/kmmw43j2z6.2 for details), DAPI spots 5-20 μm close to the Surface were identified as $CD11b^+$, $Arg1^+$, and/or $CD206^+$ using the Find Spots Close to Surface function in Imaris. To identify $CD11b^+$ $Arg1^+$ or $CD11b^+$ $CD206^+$ double positive cells, the Colocalize Spots function selecting CD11b -and Arg1-positive spots or CD11b- and CD206-positive spots, respectively, with a threshold of =<1 μm was used in Imaris.

Ex vivo experiments of primary skin fibroblast and bone marrow-derived macrophages (BMDMs)

Primary skin fibroblast isolation

6-12 week old C57BL/6 mice were euthanized and their ventral skin covering the thorax was shaved and residual hair were removed by NAIR application. The skin was excised and remaining subcutaneous fat was removed before the tissue was finely minced with scissors. The tissue was then transferred into a 2 ml tube containing 1 ml of digestion medium (2 mg/ml collagenase XI, 0.5 mg/ml hyaluronidase, 0.1 mg/ml DNase in RPMI with 10% FBS, 2 mM L-glutamine, 100 U/ml penicillin, 100 μg/ml streptomycin, 50 μM beta-mercaptoethanol). Tissue from one skin excision was split into 3 tubes. The tubes were placed horizontally in a bacterial shaker for 90 min at 37°C and 225 rpm. After digestion, the samples were filtered on a 100 μm cell strainer and the digestion was quenched by adding 20 ml of ice cold RPMI. The single cell suspension was then seeded at a concentration of $2x10^4$ cells / cm^2 in fibroblast media (DMEM supplemented with 10% FBS, 2 mM L-glutamine, 50 μM beta-mercaptoethanol, 100 U/ml penicillin, 100 μg/ml streptomycin, and 250 ng/ml amphotericin B) at 37°C in 5% CO_2. After 3 days or when culture reached 80-90% confluency, cells were collected, aliquoted, and stored in liquid nitrogen (passage 1). For subsequent co-culture experiments, cells were thawed and cultured in fibroblast media for one more passage before use in experiments.

Generation of bone marrow-derived macrophages (BMDMs)

6-12 week old C57BL/6 mice were euthanized and their femurs and tibiae were excised. Using PBS, the bone marrow was flushed from the long bones after cutting off the ends. After pelleting the bone marrow, the red blood cells were lysed using RBC lysis buffer (155 mM NH_4Cl, 12 mM $NaHCO_3$, 0.1 mM EDTA) for 5 min at RT. Cells were washed with DMEM and filtered through a 40 μm cell strainer before being seeded at $1x10^6$ cells / ml on a low-adherent cell culture dish in BMDM media (DMEM supplemented with 10% FBS (Benchmark), 2 mM L-glutamine, 50 μM beta-mercaptoethanol, 100 U/ml penicillin, 100 μg/ml streptomycin, and 20 ng/ml M-CSF). After 3 days in culture, cells were split 1:2 into new low-adherent cell culture dishes with fresh BMDM media. On day 6-7 of culture, BMDMs were harvested and used for experiments.

For Oncostatin M stimulation, PSF's were grown to 80% confluency, before switching to DMEM+1% FBS with 50 ng/mL of recombinant OSM (Biolegend) and incubated 24hrs at 37C before harvest for RNA extraction.

Conditioned BMDM media from $Grn^{-/-}$ was generated as follows: BMDM's were generated as described above from bone marrow from $Grn^{-/-}$ mice. On D7 following BMDM isolation and differentiation, the media was replaced with DMEM+1%FBS and harvested 24 hours following incubation. PSF's were grown till 80% confluent then media was replaced with $Grn^{-/-}$ BMDM CM with or without 1 ug/mL recombinant Progranulin (R&D). PSF's were incubated at 37C for 24hrs before harvest for RNA extraction.

For Periostin treatment, Collagen IV coated 6 well plates (Corning 354428) were coated with 1 ug/mL recombinant mouse Periostin (R&D 2955-F2-050) overnight at 4C. Plates were then washed twice with PBS before cell plating. BMDM's D8 post-isolation and differentiation were then plated at a density of 750k cells per well and briefly spun down at 200g for 15 seconds to force them into contact with the plate. BMDM's were then incubated 24 hrs at 37C before RNA extraction.

Reverse transcription real-time quantitative PCR

Following cell harvest and washing 1X cold PBS, cells were lysed and RNA extraction performed using the RNeasy kit from Qiagen. Roughly equal mass of RNA was then used for reverse transcription using the iScript Master Mix. The reaction mix was directly used for RT-qPCR with the SsoFast EvaGreen kit and read out on a Bio-Rad thermocycler with the following cycling protocol: [95C for 30s, 95C for 5s, 60C for 2s, repeat from step 2 44x, 65C to 95C melt curve with 0.5C increments at 5s each]. Primer sequences can be found in the key resources table. We confirmed that melt curves were consistent across samples and the non-template controls has no appreciable amplification. Cq was calculated at roughly ¼ the maximum signal and then corrected against 18s Cq before conversion to relative expression. Shown bar charts are representative of the mean+SE of 3 technical replicate wells.

QUANTIFICATION AND STATISTICAL ANALYSIS

Statistical details of individual experiments can be found in their respective figure legends.

Quantification of cells in microscopy images

Quantification in whole-mount wounds

To quantify the number of cells per area of wound in the Imaris software, first, a user-defined 'center' spot was selected in the wound that represents the center of the wound. This spot was duplicated to create a new spot object. Then, the duplicated 'center' spot was selected and using the 'Distance Transformation' tool under 'Tools -> Create new Channel' a new channel was generated, wherein the channel intensity across the sample reflects the distance from the previously selected center spot. Areas close to the center spot have a low intensity and areas distant from the center have a high intensity in the 'Distance Transformation' channel. To calculate how many cells/spots are located at what distance from the center of the wound, the 8 mm wound cutout used for imaging was subdivided into 8 circular bins (0-0.5 mm distance from center of wound; 0.5-1.0; 1.0-1.5; 1.5-2.0; 2.0-2.5; 2.5-3.0; 3.0-3.5; 3.5-4.0). Cells/spots with a cell marker of interest was selected, for example 'CD11b+' spots, and a new filter was created called 'Intensity Mean' of the 'Distance Transformation' channel. Selection of the maximum and minimum filter settings reflect which of the 8 circular bins all 'CD11b+' spots are counted. The same was done for all 'CD11b+ Arg1-tdTomato+' spots and the percentage of 'CD11b+ Arg-tdTomato+ of CD11b+' spots was calculated for each of the 8 circular bins and plotted. The same analysis was done for 'CD11b+ CD206+' spots.

Quantification in thick and thin wound and tumor cryosections

To quantify the distance of cells to POSTN or Selectin-P or CD31 surfaces, we used surfaces generated using parameters listed in the Imaris parameters table (see Mendeley data at https://doi.org/10.17632/kmmw43j2z6.2) and created a distance transform channel from the outside of these surfaces. The value of this channel at the center of the cells/spots was used as the distance value in histograms and distributions for KS testing.

Space/Time Tileplot of cell frequencies

To depict the distribution of identified cell subsets in the scRNAseq data set within the wound over time, we devised a Space/Time Tileplot that is a 4x4 grid, where the x-axis is split into the four time points of sampling (day 1, day 3, day 7, and day 14) and the y-axis is split into the four areas of the sampled wound (2 mm wound center, 4 mm ring, 6 mm ring, 8 mm ring). This generates 16 space/timepoints. To plot the tileplot, we used the 'geom_tile' function from the ggplot2 R package. First, each cell cluster's percentage within a larger object (for example the 'Mono_Mac_1' cluster within the larger 'Mono_Mac' object) is calculated for each space/timepoint. These are then plotted on the 4x4 grid and color-coded based on their relative change compared to the unwounded state. Red indicates increase in subpopulation, white indicates the same percentage, blue indicates decrease in subpopulation compared to UW. Code is deposited and provided.

Space/Time Correlation Analysis (STCA)

To identify cell subsets in the scRNAseq data set that shared similar space/time profiles, we calculated the Pearson correlation coefficient, R, using the percentage for every space/timepoint between pairs of cell subsets. A Pearson correlation coefficient of $R = 1$ between a pair of cell subsets would indicate that they have the same space/time profile across the wound healing process. A Pearson correlation coefficient of $R = -1$ would indicate an negative correlation between the cell subsets, i.e. that the presence of the two cell subsets are inversely correlated across the wound. P-values were calculated using either Pearson or Spearman method (noted in legends). The Benjamini-Hochberg correction was applied for false discovery rate correction.

NMF Decomposition

The CD45-/+ objects were subsetted according to broad cell type definitions (M/M, Neutrophils, DC's, Mast Cells, T, TNK, B and Fibroblast, Keratinocyte, Endothelial, Melanocyte, Dermal sheath papilla, vSM). The top 1250 most variable genes (depending on diversity of subset expression patterns) were selected using the 'vst' method in Seurat. Using the scaled RNA assay (non-centered) and subsetting out the most variable genes, we thus created a 1250xN (N = # of cells) expression matrix, then applied the non-smooth NMF algorithm (as described in NMF package[101]). We used a parameter sweep combined with the cophenetic metric to find the most stable number of factors using 50 iterations.

For gene weights per factor, we used the basis matrix output from the nsNMF and sorted based on the highest contributing genes. For plotting purposes, we normalized gene contributions across all factors to understand how specific a given gene was for a factor. We used the coefficient matrix as the 'expression' value for each cell for that factor. This value was used directly for average factor expression and feature plots.

When translating factors between tumor and wound healing, we used a Jaccard distance metric based on the top 20 contributing genes for each factor.

$$J_{20} = ((\textit{top 20 genes factor } n) \cap (\textit{top 20 genes factor } m))/(\textit{top 20 genes factor } n \cup \textit{top 20 genes factor } m)$$